HHS Public Access

Author manuscript

Cell Rep. Author manuscript; available in PMC 2022 October 25.

Published in final edited form as:

Cell Rep. 2022 October 04; 41(1): 111444. doi:10.1016/j.celrep.2022.111444.

A non-canonical retina-ipRGCs-SCN-PVT visual pathway for mediating contagious itch behavior

Fang Gao[1,2], **Jun Ma**[1,2], **Yao-Qing Yu**[1,2,3], **Xiao-Fei Gao**[1,2,8], **Yang Bai**[1,4,9], **Yi Sun**[1,4,10], **Juan Liu**[1,2], **Xianyu Liu**[1,2], **Devin M. Barry**[1,2], **Steven Wilhelm**[1,2], **Tyler Piccinni-Ash**[1,2], **Na Wang**[1,2,11], **Dongyang Liu**[1,2,7], **Rachel A. Ross**[5], **Yan Hao**[1,2,12], **Xu Huang**[6], **Jin-Jing Jia**[1,2,13], **Qianyi Yang**[1,2], **Hao Zheng**[6], **Johan van Nispen**[1,2,14], **Jun Chen**[3], **Hui Li**[4], **Jiayi Zhang**[6], **Yun-Qing Li**[4], **Zhou-Feng Chen**[1,2,15,*]

[1]Center for the Study of Itch and Sensory Disorders, Washington University School of Medicine, St. Louis, MO 63110, USA

[2]Departments of Anesthesiology, Medicine, Psychiatry and Developmental Biology, Washington University School of Medicine, St. Louis, MO 63110, USA

[3]Institute for Biomedical Sciences of Pain, Tangdu Hospital, Fourth Military Medical University, Xi'an 710038, P. R. China

[4]Department of Anatomy, Histology and Embryology & K.K. Leung Brain Research Centre, Fourth Military Medical University, Xi'an 710032, P. R. China

[5]Department of Neuroscience, Psychiatry and Medicine, Albert Einstein College of Medicine Rose F. Kennedy Center, Bronx, NY, USA

[6]Institutes of Brain Science, State Key Laboratory of Medical Neurobiology, MOE Frontiers Center for Brain Science and Institute for Medical and Engineering Innovation, Eye & ENT Hospital, Fudan University, Shanghai 200031, P.R. China

[7]Department of Pain Management, the State Key Clinical Specialty in Pain Medicine, the Second Affiliated Hospital, Guangzhou Medical University, Guangzhou 510260, P.R. China

[8]Present address: Translational Research Institute of Brain and Brain-like Intelligence, Shanghai Fourth People's Hospital, School of Medicine, Tongji University, Shanghai 200434, P. R. China

[9]Present address: Department of Neurosurgery, General Hospital of Northern Theater Command, Shenyang 110016, P. R. China

[*]Correspondence: chenz@wustl.edu.

AUTHOR CONTRIBUTIONS

F.G. performed most experiments, including ablation, immunostaining, viral tracing, chemogenetics, optogenetics, *in vivo* Ca^{2+} imaging, and behavioral experiments. J.M. conducted *in vivo* extracellular recording of SCN GRPR neurons. F.G. and J.M. conducted data analysis. Y.-Q.Y. performed ipRGC ablation studies. X.-F.G. performed slice electrophysiological recording. J.L. and Q.Y. performed RNAscope, X.L., D.M.B., T.P.-A., S.W., N.W., Y.H., X.H., J.-J.J., H.Z., Y.H., Y.B., Y.S., and J.v.N. participated in behavioral tests. J.C., H.L., and Y.-Q.L., for helping with this project, J.C. and J.Z. contributed to behavioral tests and discussion. R.A.R. generated *Adcyap1*$^{f/f}$ mice. F.G., J.M., and Z.-F.C. wrote the manuscript, and Z.-F.C. conceived and supervised the project.

DECLARATION OF INTERESTS

The authors declare no competing interests.

SUPPLEMENTAL INFORMATION

Supplemental information can be found online at https://doi.org/10.1016/j.celrep.2022.111444.

[10]Present address: Binzhou Medical University, Yantai 264003, P. R. China

[11]Present address: Shandong Provincial Hospital for Skin Diseases & Shandong Provincial Institute of Dermatology and Venereology, Shandong First Medical University & Shandong Academy of Medical Sciences, Jinan, P. R. China

[12]Present address: Department of Pediatrics, Tongji Hospital, Tongji Medical College, HuaZhong University of Science and Technology, Wuhan 430030, P. R. China

[13]Present address: College of Life Sciences, Xinyang Normal University, Xinyang 464000, P. R. China

[14]Present address: Saint Louis University School of Medicine, St. Louis, MO 63104, USA

[15]Lead contact

SUMMARY

Contagious itch behavior informs conspecifics of adverse environment and is crucial for the survival of social animals. Gastrin-releasing peptide (GRP) and its receptor (GRPR) in the suprachiasmatic nucleus (SCN) of the hypothalamus mediates contagious itch behavior in mice. Here, we show that intrinsically photosensitive retina ganglion cells (ipRGCs) convey visual itch information, independently of melanopsin, from the retina to GRP neurons via PACAP-PAC1R signaling. Moreover, GRPR neurons relay itch information to the paraventricular nucleus of the thalamus (PVT). Surprisingly, neither the visual cortex nor superior colliculus is involved in contagious itch. *In vivo* calcium imaging and extracellular recordings reveal contagious itch-specific neural dynamics of GRPR neurons. Thus, we propose that the retina-ipRGC-SCN-PVT pathway constitutes a previously unknown visual pathway that probably evolved for motion vision that encodes salient environmental cues and enables animals to imitate behaviors of conspecifics as an anticipatory mechanism to cope with adverse conditions.

In brief

It has been shown that GRP-GRPR neuropeptide signaling in the SCN is important for contagious itch behavior in mice. Gao et al. find that SCN-projecting ipRGCs are sufficient to relay itch information from the retina to the SCN by releasing neuropeptide PACAP to activate the GRP-GRPR pathway.

Graphical Abstract

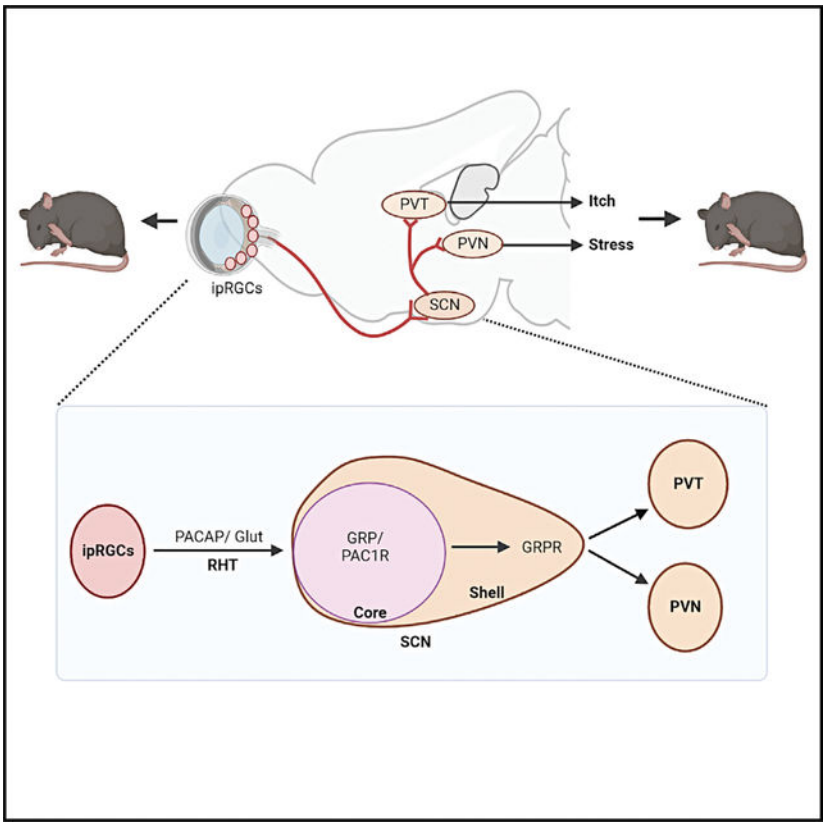

INTRODUCTION

Animals scan, recognize, and extract salient information from a complex visual world to guide their behaviors for survival (Desimone and Duncan, 1995; Itti and Koch, 2001). Aside from direct observation of the environment, social animals infer and adapt to ever-changing challenging conditions by watching and copying the behavior of group-living conspecifics, which may forecast potential danger or risk that is difficult to detect by direct visual inspection. Such involuntary imitation of the motor behavior of conspecifics is referred to as socially contagious behavior or automatic mimicry and can be distinguished from social imitation that relies on social learning and reward (Zentall, 2006). Contagious behavior is thought to be mediated by a built-in innate circuitry formed during evolution, and it facilitates social bonding and affiliation by enabling social animals to act in synchrony (Hatfield et al., 1994; Lakin et al., 2003; Prochazkova and Kret, 2017). Contagious behavior is a primitive form of emotional contagion with adaptive value crucial for the survival of social animals (de Waal and Preston, 2017; Hatfield et al., 1994; Mogil, 2019). Itch contagion is present in several animal species, including humans (Provine, 2012) and nonhuman primates (Schut et al., 2015). In mice, contagious itch behavior (CIB) was discovered when wild-type (WT) mice housed with those with chronic itch also exhibited higher spontaneous scratching behavior (Yu et al., 2017). Using an LED monitor that displays mouse scratching behavior, observing mice were found to imitate scratching behavior (Yu et al., 2017). The CIB test was replicated to show that a mouse model of

autism displayed profound deficits in CIB (Gonzales-Rojas et al., 2020). The discovery of itch contagion in mice provides a unique opportunity for unraveling the underlying mechanisms, and its ethological significance.

Gastrin-releasing peptide (GRP) in somatosensory neurons encodes itch-specific information and can activate GRPR, a G_q protein-coupled receptor (GPCR), in the spinal cord to transmit itch information in mice (Barry et al., 2020; Chen, 2021; Sun and Chen, 2007; Sun et al., 2009). GRP is conserved across animal phyla, including mammals (Hirooka et al., 2021; Takanami et al., 2022). Suprachiasmatic nucleus (SCN) GRP neurons are a subset of retinorecipient cells located in the ventrolateral side (the core area) and convey photic information directly from the retinohypothalamic tract (RHT) (Abrahamson and Moore, 2001; Karatsoreos et al., 2004). We previously found that SCN GRP-GRPR signaling is crucial for mediating CIB (Yu et al., 2017). Our studies hint at the possibility that intrinsically photosensitive retina ganglion cells (ipRGCs), a third class of light-sensitive photoreceptors expressing melanopsin, a light-sensing photopigment required for photoentrainment of circadian rhythm (Lucas et al., 2003; Provencio et al., 1998; Ruby et al., 2002), as an input conduit that acts upstream of SCN GRP neurons. However, it is well established that SCN-projecting ipRGCs are exclusively dedicated to non-imaging-forming function, since the intrinsic photosensitivity of ipRGCs mediated by melanopsin is optimally responsive to ambient light over sustained timescales (hours or days) (Berson et al., 2002; Lucas et al., 2020; Schmidt et al., 2011). While ipRGCs can contribute to some aspects of image-forming vision, this role is attributed to their projection to the canonical visual pathways, such as the superior colliculus (SC) and dorsal lateral geniculate nucleus (dLGN) (Ecker et al., 2010; Lucas et al., 2020). The fact that the scratching demonstrator represents a fast-moving motion stimulus (Gonzales-Rojas et al., 2020; Yu et al., 2017) indicates the necessity for the classic rods and cones in mediating CIB. Indeed, motion vision in primates and rodents has been shown to be mediated exclusively through the canonical visual pathways originating in the rods/cones (Borst and Euler, 2011; Ito and Feldheim, 2018; Marques et al., 2018; Niell and Stryker, 2010; Wang et al., 2020).

In this study, we set out to address the discrepancies between our finding and the current understanding of the visual systems. Using an array of approaches, we uncover the retina-ipRGCs-SCN-PVT neural pathway as a previously unknown visual pathway for conveying contagious itch information, independently of melanopsin.

RESULTS

Contagions itch encodes salient stressful information

The ecological and physiological importance of CIB remains a matter of speculation (Provine, 2012; Schut et al., 2015). To determine whether scratching motion may encode negative valence, we examined the stress and anxiety-like response of mice using the open-field and light-dark box tests after the CIB test (Figures S1A and S1E). Compared with the control mice exposed to the video showing an ambulating demonstrator, mice exposed to the scratching video entered the center less frequently and spent less time in the center in the open field as well as in the light box (Figures S1B–1D and S1F), suggesting that scratching video encodes stressful information. Consistent with that acute

stress induces thermal analgesia (Butler and Finn, 2009), we found a significant increase in the threshold for thermal pain in observing mice exposed to the scratching video (Figures S1G and S1H). The reduced thermal pain was normalized by intraperitoneal (i.p.) injection of CP154,526, the selective antagonist of corticotropin-releasing factor 1 receptor used to dampen stress response (Overstreet et al., 2004) (Figure S1H). Similarly, the scratching video also increased the corticosterone level, which was blocked by CP154,526 (Figure S1I). These results demonstrate that the scratching motion conveys socially transmitted stressful information.

SCN-projecting ipRGCs are required for CIB

To explore the upstream mechanisms of CIB, we performed Cre-dependent virus-mediated retrograde monosynaptic tracing in the SCN of *Grp*^{Cre} mice using the RV-ENVA-ΔG-dsRed as monosynaptic tracer following the helper AAV expressing RmL), control virus AAV5-EF1a-DIO-eYFP and TVA (Figures S2A and S2B). Consistent with early studies (Moore et al., 2002; Fernandez et al., 2016), we found that most of the monosynaptic contacts between the retina and SCN GRP neurons express melanopsin (Figures S2C–S2F), indicating the direct projection from ipRGCs to SCN GRP neurons.

Next, we performed chemogenetic inhibition of ipRGCs by bilateral intravitreal injection of *Opn4*^{Cre} mice with Cre-dependent virus encoding Gi-coupled designer receptor activated by designer drugs (DREADDs), hM4Di (AAV-hSyn-DIO-hM4D(Gi)-mCherry) or AAV-hSyn-DIO-eYFP as a control (Figures 1A and 1B). Clozapine treatment (i.p. injection) significantly attenuated CIB of mice expressing Gi in ipRGCs (Figures 1C–1E). In contrast to diminished GRP immunostaining after the CIB test (Yu et al., 2017), GRP was normal after clozapine treatment (Figures 1F and 1G), indicating that chemogenetic inhibition prevents GRP release during the CIB test. Moreover, bilateral intravitreal injection of melanopsin-saporin (Mel-sap), which nearly ablated all ipRGCs (Figures S3A–S3C), resulted in profound deficits in CIB (Figures S3D and S3E). Consistent with previous studies (Goz et al., 2008), Mel-sap did not affect the other types of retinal cells, including PKCα, a marker for rod bipolar cells (Ruether et al., 2010), PKCβ, a marker for cone bipolar cells (Kolb et al., 1993), and RBPMS, a pan-retina ganglia cell marker (Tran et al., 2019) (Figure S3F). To explore whether SCN-projecting ipRGCs are directly involved in CIB, a retrovirus expressing Cre recombinase (RetroAAV-Ef1α-mCherry-IRES-Cre) was injected into the SCN of C57BL/6J mice for a subsequent 3 weeks to allow for Cre expression, followed by intravitreal injection of Cre-dependent Gi virus (AAV-hSyn-DIO-HA-h4MD(Gi)-IRES-mCitrine) (Figures 1H–1K). The selective chemogenetic inhibition of SCN-projecting ipRGCs markedly attenuated CIB without affecting look behavior (Figures 1L and 1M). Interestingly, there are no significant differences in imitative scratching between WT and mice lacking *Opn4* (*Opn4* KO) (Figures 1N and 1O). These findings indicate that SCN-projecting ipRGCs constitute a pivotal visual conduit for relaying itch information into SCN GRP neurons independently of melanopsin.

Optostimulation of ipRGC terminals in the SCN, but not dLGN or SC, evokes itch-related scratching behavior

To test whether the direct projection of ipRGCs to the SCN is capable of mediating CIB, we employed a strategy that permits selective activation of ipRGC terminals in the SCN without concurrent activation of extra-SCN areas. The right eye of *Opn4*^{Cre} mice was injected with a Cre-dependent viral vector encoding channel rhodopsin (AAV-Syn-DIO-hChR2 (H134R)-eYFP) (ChR2) (Figures 2A and S4A). Overlapping expression of melanopsin and anterogradely transported ChR2-eYFP was detected ipsilaterally, but not contralaterally, in the eye, confirming the success of the injection (Figure S4B). Extra ChR2-eYFP expression was also detected, as well as the overlap with melanopsin, indicating that the *Opn4*^{Cre} line is not specific. However, this non-specific expression effect can be circumvented by selective stimulation of ipRGC terminals from within the SCN, which received direct ipRGCs input fromthe eye (Baver et al., 2008). Extensive co-localization between ChR2-eYFP and GRP in the ventral side of the SCN was detected by immunohistochemistry (IHC) (Figure 2C), further confirming direct contacts between terminals of ipRGCs and GRP neurons. Optical fibers were then inserted into the left side of SCN of eYFP control and ChR2 mice, followed by blue light stimulation (473 nm, 10 mW power from fiber tip) (Figures 2A and 2B). Similar to optostimulation of SCN GRP neurons (Yu et al., 2017), 5 or 10 Hz evoked scratching behavior in ChR2 mice but not in eYFP control mice (Figures 2D and 2E; Video S1).

Consistent with our study (Yu et al., 2017), ablation of SCN GRPR neurons of ChR2 mice with bombesin-sap (BB-sap) significantly attenuated the scratching behavior evoked by 5 and 10 Hz blue light stimulation (Figures 2D, 2E, S4C, and S4D), indicating that scratching behavior evoked by optostimulation requires GRPR neurons. By contrast, optostimulation of the dLGN or SC-projecting ipRGCs of *Opn4*^{Cre} mice expressing ipRGC-ChR2 failed to evoke significant scratching behavior (Figures 2F–2K).

The visual cortex and SC are not required for CIB

The aforementioned results prompted us to evaluate the role of the visual cortex in CIB, and we first examined CIB of “cortexless” mice in which *Tra2β* (alternative splicing factor transformer 2 beta) was conditionally deleted during development, resulting in the loss of the dLGN-V1 pathway without impairing the SC (Shanks et al., 2016). Surprisingly, *Tra2β* conditional knockout (CKO) mice showed a dramatic increase in the look behavior (Figures S5A and S5C), an indicator of enhanced attention to the scratching motion, probably resulting from a lack of primary visual cortex-mediated top-down inhibition (Kaneda et al., 2012). In accordance with the fact that CIB is the function of look behavior (Yu et al., 2017), CIB of *Tra2β* CKO mice increased significantly (Figure S5B). To ascertain whether enhanced CIB may be ascribed to potential developmental compensation in *Tra2β* CKO mice, the entire visual cortex of C57BL/6J adult mice was bilaterally aspirated without damaging dLGN or SC (Figures 3A, S5D, and S5E), which was functionally verified by a lack of depth perception using the visual cliff test (Figures 3D and 3E). Remarkably, these lesioned mice showed normal CIB (Figures 3B and 3C). We also ablated SC, an evolutionarily ancient visual pathway in rodents (Ito and Feldheim, 2018), which was verified by deficits in freezing behavior as measured using the sweeping test (De Franceschi

et al., 2016) (Figures 3I–3J and S5F–S5G). Despite slightly reduced look behavior in the CIB test (Figure 3G), SC lesioned mice could still imitate scratching behavior (Figure 3H).

PACAP transmits contagious itch information via PAC1R

We next asked whether PACAP encoded by *Adcyap1*, a principal neuropeptide that relays photic information from the RHT to the SCN (Hannibal et al., 1997, 2000), may mediate CIB. To visualize the contacts between PACAPergic fibers and GRP neurons, AAV-hSyn-DIO-eYFP virus was intravitreally injected into the eyes of *Adcyap1*^{Cre} mice (Figure 4A), and IHC studies revealed substantial overlapping between eYFP terminals and GRP in the ventrolateral SCN (Figure 4B), indicating direct projection of retinal PACAP-expressing neurons to the SCN.

PAC1 receptor (PAC1R), a cognate receptor for PACAP, is broadly expressed in SCN, including the ventrolateral area innervated by PACAP fibers (Hannibal et al., 1997). Although VPAC2 receptor encoded by the *VIPR2* gene is closely related to PAC1R, it is worth noting that PACAP/PAC1R functions independent of VIP/VPAC2 with PAC1R and VPAC2 or GRP and VIP are expressed in distinct populations of SCN neurons (Hannibal et al., 2017). RNAscope ISH showed that approximately 70% of *Grp* neurons express *Adcyap1r1*, which encodes PAC1R (Figures 4C and 4D). To test whether PACAP may activate *Grp*/PAC1R neurons, *Grp*^{Cre} mice were mated with Ai9 tdTomato reporter line to generate *Grp*$^{Cre/tdTomato}$ mice that could permanently label *Grp* neurons with tdTomato marker, referred to as *Grp*^{tdTom} neurons (Barry et al., 2020).

Whole-cell recording of SCN *Grp* neurons in brain slices obtained from *Grp*^{tdTom} mice showed that PACAP significantly increased glutamate-mediated inward current in *Grp*^{tdTom} neurons (Figures 4E–4G). This finding is in agreement with previous reports showing that PACAP and glutamate are co-released from the terminals of SCN-projecting RHT to regulate SCN neurons (Chen et al., 1999; Hannibal et al., 2000) through enhanced AMPA, and NMDA evoked Ca^{2+} transients (Michel et al., 2006).

We next conditionally deleted *Adcyap1* by bilateral intravitreal injection of AAV-Syn-Cre-IRES-GFP virus in *Adcyap1*$^{f/f}$ mice (Figure 4H). Retina-specific deletion of *Adcyap*, confirmed by qRT-PCR (Figure 4I), resulted in pronounced deficits in CIB without affecting the look behavior (Figures 4J and 4K). To ablate SCN neurons expressing PAC1R, we injected PACAP-saporin (PACAP-sap) into the SCN, which diminished *Adcyap1r1* expression (Figures 5A–5C). Ablation of PAC1R neurons profoundly reduced CIB (Figures 5D and 5E). The specificity of PACAP-sap was also verified by reduced GRP, but not AVP or VIP expression (Figures S6A and S6B). To determine the role of PAC1R in CIB, we injected *Adcyap1r1* siRNA into the SCN (Figure 5F). As expected, A*dcyap1r1* knockdown also dramatically diminished CIB (Figures 5G–5J).

Contagious itch stimuli activate GRPR itch neurons

Next, we examined the somatic Ca^{2+} activity dynamics of SCN GRPR neurons using *in vivo* microendoscopic deep brain imaging in freely behaving *Grpr*^{iCre} mice during the CIB test (Figures 6A–6D). RNAscope ISH indicated that approximately 93% of SCN *iCre* neurons of *Grpr*^{iCre} mice express *Grpr*, confirming the high fidelity of *Grpr*^{iCre} mice (Figures S7A

and S7B). The SCN of *Grpr*^{iCre} mice was first injected with Cre-dependent virus expressing calcium sensor GCaMP6s (AAVDJ-EF1α-DIO-GCaMP6s). Ca^{2+} activity of SCN GRPR neurons was imaged at single-cell resolution through a miniaturized integrated fluorescence microscope mounted on the head of a mouse with a graded index (GRIN) lens implanted above the SCN during the CIB test (Figures 6A–6D; Video 2). Unlike imaging of the superficial brain, a strong motion severely impeded the Ca^{2+} imaging of a tiny SCN at the base of the hypothalamus. To overcome the problem, we manually selected regions of interest to analyze the Ca^{2+} fluorescence of individual GRPR neurons and carefully rechecked the raw images. This method allowed us to obtain stable Ca^{2+} signals for analysis by eliminating the motions that cannot be corrected by the algorithm in the raw images (Video S3).

Owning to a delay of imitative scratching behavior after look (Yu et al., 2017), we limited our analysis of Ca^{2+} activity of GRPR neurons to the timescale between the onset of look and imitative scratching behaviors (0–4 s) to avoid the potential feedback influence resulting from imitative scratching itself (Morin and Allen, 2006; Schaap and Meijer, 2001). In the ambulating demonstrator or control group, 16 out of 161 GRPR neurons (9.9%) were activated based on an increase of Ca^{2+} signal (Figures 6F and 6I), suggesting that a small fraction of GRPR neurons was tuned to the motion of ambulating conspecifics. For scratching demonstrators, we classified the Ca^{2+} activity of GRPR neurons according to two types of behaviors: look without ensuing scratching behavior, referred to as look-without-scratch, and look followed by imitative scratching behavior, referred to as imitative scratch. A total of 34 GRPR neurons (21.7%) in the look-without-scratch group were activated (Figures 6G and 6J). Importantly, the number of neurons showing excitatory response increased to 45 (28.0%) in the imitative scratch group (Figures 6H and 6K). By contrast, these 45 GRPR neurons showed no activated Ca^{2+} activity in the control look or the look-without-scratch group (Figures S7E–S7H). The percentage of activated GRPR neurons is significantly higher in the imitative scratch group than the control look and look-without-scratch groups (Figure 6L). Moreover, the mean Ca^{2+} activity of the activated GRPR neurons induced by the look behavior in the imitative scratch group (45 neurons) is significantly higher than that in the control look (16 neurons) and look-without-scratch groups (34 neurons) (Figure 6M). Conversely, there is a steady decrease in the proportion of GRPR neurons that were inhibited from the control look (41.0%), look-without-scratch (31.7%), to imitative scratch (24.2%) (Figures 6I–6K and S7C). Of note, approximately half of GRPR neurons did not respond to the demonstrators, regardless of the type of the demonstrator (Figures 6I–6K and S7D). Together, these findings demonstrate that a substantial portion of GRPR neurons is preferentially activated by scratching motion.

GRPR itch neurons display unique firing patterns

To examine the firing patterns of itch-sensitive GRPR neurons at a high temporal resolution during the CIB test, we performed *in vivo* multichannel extracellular recording of SCN GRPR neurons in freely moving mice during the CIB test (Figures 7A–7C; Video S4). A self-made optrode, consisting of eight tetrodes and one optic fiber, was implanted into the SCN of *Grpr*^{iCre}; Ai32 mice so that SCN GRPR neurons could be identified based on light sensitivity using optogenetics (Figures 7C and 7D). To identify GRPR neurons,

we applied a brief blue light pulse (20 Hz, 1ms) to elicit short-latency action potentials. Spike sorting yielded 159 well-isolated single units from *Grpr*^{iCre}; Ai32 mice (n = 7) for an optical-tagging test (SALT) (Kvitsiani et al., 2013) (Figures 7F and 7G). This test identified a total of 88 GRPR neurons ($p < 0.01$; SALT test for optogenetic identification; Figures 7E–7G). GRPR neurons possess relatively low baseline firing rates (Figure 7H), with a vast majority (94.3%) being less than 10 Hz, while 68.2% were lower than 4 Hz. These findings are consistent with previous recordings of SCN neurons (Brown et al., 2008; Lalic et al., 2020; Mazuski et al., 2018; Welsh et al., 1995).

Next, we asked whether there is a correlation between the firing rates of SCN GRPR neurons and scratching motion inputs by examining the peri-event time histograms (PETHs) of the firing rates during the same timescale (−5 to 5 s) across three behavioral groups. Of 88 GRPR neurons identified, the majority are non-responders (60.2%; n = 53) (Figure 7K). While a small fraction was inhibited (10.2%; n = 9), 26 GRPR neurons (29.5%) showed increased excitatory responses in the imitative scratch group (Figures 7K and 7L). By contrast, only six GRPR neurons (11.4%) in the look-without-scratch group and one GRPR neuron (4.5%) in the control look group were activated (Figures 7I, 7J, and 7L). To further analyze the population activity of identified individual GRPR itch-sensitive neurons in the CIB test, a comparison of normalized firing rates of 26 GRPR neurons showed a significant increase after the look compared with before the look behavior in the imitative scratch group (Figures S8A–S8C). By contrast, 26 GRPR neurons showed no significant increases in normalized firing rates in the control look and the look-without-scratch groups (Figures S8B and S8C). Therefore, 26 GRPR neurons are hereinafter referred to as GRPR itch neurons. At last, we compared the PETHs of the firing rates for GRPR itch neurons 5 s before and after look (−5–0 s, 0–5 s) across three behavioral conditions. Interestingly, the control group shows a decreased firing rate (1.88 ± 0.35 vs 1.62 ± 0.35 Hz) (Figure S8D). While the mean firing rates remain the same in the look-without-scratch group (1.79 ± 0.55 vs 1.8 ± 0.54 Hz) (Figure S8E), there is a significant increase in the imitative scratch group (0.78 ± 0.26 vs 1.72 ± 0.41 Hz) (Figure S8F). Intriguingly, the average baseline firing rate of GRPR itch neurons (−5–0 s) before look is significantly lower (0.78 ± 0.26 Hz) when compared with the two control groups (Figure S8G), suggesting a transient suppression of firing rates prior to the onset of look behavior. This finding prompted us to compare the firing rates between GRPR itch and non-itch neurons to identify the features unique to GRPR itch neurons. As expected, the average normalized firing rate of GRPR itch neurons is significantly increased compared with GRPR non-itch neurons (n = 62) in the imitative group (Figure S9A). Notably, the overall mean firing rate of GRPR itch neurons is significantly lower than GRPR non-itch neurons (1.72 ± 0.39 vs 4.42 ± 0.55 Hz) (Figures S9B–S9E). A suppression (0.78 ± 0.26 Hz) of the baseline firing rate of GRPR itch neurons occurred only in the imitative scratch group, but not in the two control groups (1.88 ± 0.35 vs 1.79 ± 0.55 Hz vs 1.72 ± 0.39 Hz). By contrast, GRPR non-itch neurons lack the suppression across all three behavioral conditions (5.33 ± 0.73 vs 5.37 ± 0.81 Hz vs 5.59 ± 0.84 Hz) (Figure S9F). Importantly, GRPR non-itch neurons also displayed a reduced firing rate in the control look group (5.33 ± 0.73 vs 5.05 ± 0.68 Hz) (Figure S9G), suggesting that this suppression may reflect an overall feedback inhibition of GRPR neurons related to the look behavior. No significant differences were observed in the mean firing rate for GRPR

non-itch neurons in the look-without-scratch group (5.37 ± 0.81 vs 5.3 ± 0.79 Hz) (Figure S9H) and the imitative scratch group (5.59 ± 0.84 vs 5.34 ± 0.8 Hz) (Figure S9I). These results demonstrate that GRPR itch neurons possess unique electrophysiological features that are highly correlated with scratching motion input.

GRPR neurons relay itch information through their projection to the PVT

Finally, we sought to explore the output circuits of SCN GRPR neurons by performing whole-brain output mapping. Injection of Cre-dependent virus encoding eGFP (AAV-hSyn-DIO-eGFP) into the SCN of *Grpr*^{iCre} mice revealed that GRPR neurons heavily innervate a group of the midline thalamic nuclei and the hypothalamus, as well as several subcortical areas. The most abundant eGFP fibers were found in the paraventricular nucleus of the thalamus (PVT), a sensory relay station that comprises glutamatergic neurons and conveys negative valence and arousal (Barson et al., 2020; Kirouac, 2015, 2021; Penzo and Gao, 2021), and the paraventricular nucleus of the hypothalamus (PVN) that regulates stress response via the hypothalamic-pituitary-adrenocortical (HPA) axis (Figures S10A and S10B). To determine whether the PVT is required for CIB, we took advantage of the finding that *Grpr* is expressed in the PVT (Figures S10C and S10D, 89.0% ± 2.3% *iCre*$^{+}$ PVT neurons express *Grpr*) and injected Cre-dependent virus encoding G_i-coupled DREADDs, hM4Di (AAV-hSyn-DIO-hM4D(Gi)-mCherry) or AAV-hSyn-DIO-mCherry as the control into the PVT of *Grpr*^{iCre} mice (Figure S10E and S10F). Clozapine treatment significantly diminished c-Fos expression in mCherry^{+} neurons, confirming the chemogenetic inhibitory effect on the PVT *Grpr*^{iCre} neurons (Figures S10G and S10H). Strikingly, chemogenetic inhibition of the PVT *Grpr*^{iCre} neurons also markedly impaired CIB (Figures S10I and S10J), indicating that the PVT is the output station of SCN GRPR neurons.

DISCUSSION

An unexpected role of SCN-projecting ipRGCs in image-forming function

In this study, we demonstrate that ipRGCs function upstream of the SCN to convey contagious itch information, which supports the pivotal role of SCN GRP-GRPR signaling in CIB (Yu et al., 2017). This is in contrast to the textbook view that SCN-projecting ipRGCs do not mediate image-forming functions (Contreras et al., 2021; Do, 2019; Schmidt et al., 2011). Several fundamental differences between the present and past studies can account for seemingly inconsistent conclusions. First, previous studies tested the image-forming capacity in mice lacking ipRGCs using an array of visual acuity tests, all designed to evaluate image-forming functions mediated through the canonical retina-dLGN-V1/SC visual pathways (Guler et al., 2008; Hatori et al., 2008). Second, unlike featureless visual stimuli (bars, lines, edges, etc.) typically used in vision research, only in recent years have ethologically relevant visual stimuli been adopted as behavioral paradigms for vision research in mice (Huberman and Niell, 2011; Miller et al., 2022; Wei et al., 2015). Consequently, no previous studies have examined the visual response of ipRGCs to ethologically relevant motion. Third, all documented functions of ipRGCs could be attributed to melanopsin, whose intrinsic properties may constrain ipRGCs from detecting and responding to scratching motion. For example, melanopsin operates at a slow spatiotemporal timescale (hours and days) best suited for mediating photoentrainment

of the circadian rhythm (Do, 2019; Lucas et al., 2020), whereas ipRGCs detect fast-moving stimuli in seconds. Therefore, the finding that melanopsin is not required for CIB reconciles these discrepancies. Our studies reveal an unsuspected function of ipRGCs that resembles the classic RGCs in mediating motion-based visual stimuli. By implicating the extrinsic properties of ipRGCs in CIB, our analysis underscores the distinct roles of ipRGCs with respect to their melanopsin dependence and thus significantly expands the functional repertoire of ipRGCs from their classic melanopsin-mediated non-image-forming to melanopsin-independent image-forming function.

A neuropeptide signaling cascade: From the retina to GRPR neurons

The finding that PACAP activates PAC1R in GRP neurons to convey itch information further strengthens the role of SCN-projecting ipRGCs in CIB. Given the potential role of PACAP in circadian entrainment (Hannibal et al., 1997), it is possible that differential release of PACAP/glutamate from ipRGCs/RHT may underlie itch transmission and circadian entrainment, respectively. Alternatively, selective activation of a subpopulation of PAC1R/GRP itch neurons may confer the specificity of contagious itch transmission, whereas PAC1R neurons lacking GRP may mediate circadian entrainment. The fact that PACAP and GRP sequentially relay itch from ipRGCs to GRPR neurons via GRP/PAC1R neurons may partially account for the slow kinetics of contagious itch transmission, manifesting in delayed activation of GRPR neurons and CIB after the onset of look behavior. We propose that the initial transmission of contagious itch may consist of two sequential phases: the rod/cone photoreceptors in the retina may respond to scratching motion directly, followed by a cascade of neuropeptide signaling with slow kinetics upon activation of ipRGCs. On the other hand, we could not exclude the possibility that ipRGCs may respond to salient scratching inputs directly. Nonetheless, the observation that the ipRGC-SCN-PVT pathway functions as a visual conduit by the use of neuropeptides for itch signaling is reminiscent of the cutaneous somatosensory itch pathway from the skin to the spinal cord, wherein itch information is encoded and transmitted by slow-acting neuropeptides (Barry et al., 2020; Chen, 2021; Sun et al., 2009), indicating that the contagious itch visual pathway is distinct from the canonical visual pathway after itch information is processed at the retina. Furthermore, the fact that GRPR neurons convey cutaneous and visual itch, respectively, hints at their shared ancestral origin. Genetic duplication and adoption from the pre-existing spinal GRPR neural circuits could be possible mechanisms by which neural circuits of contagious itch arose during evolution (Chakraborty and Jarvis, 2015).

SCN GRPR itch neurons respond to salient contagious itch information

Through successfully recording the response of SCN neurons of freely moving mice to external stimuli in a cell-type-specific manner, we have gained crucial access to key features of GRPR itch neurons with a high temporal resolution at both population and single-cell levels under physiological conditions. Importantly, the observation that the neural dynamics of SCN GRPR itch neurons are correlated with visual itch stimuli supplies a critical piece of evidence supporting their role in CIB. The observation of a progressive increase in the proportion of activated GRPR neurons across the control look, look-without-scratch, and look-with-scratch or imitative scratch conditions, which is accompanied by corresponding decreases in the fraction of inhibited GRPR neurons, implies that a balance of excitation

and inhibition of GRPR neurons might be crucial for triggering CIB. While such change is less pronounced when the electric spiking activities of GRPR neurons are evaluated, the discrepancies may reflect both strengths and limitations of *in vivo* calcium imaging and extracellular recording approaches (Ali and Kwan, 2020).

The data presented in this study reveal several hallmarks of GRPR itch neurons. Notably, a majority of GRPR itch neurons (~76.9%) possess a low firing rate (<2 Hz), in contrast to 41.9% of GRPR non-itch neurons. Since scratching motion represents a visual stressor to the observer, maintaining GRPR itch neurons at a lower firing rate or a quiescent state might minimize the risk of accidental firing that may result in an aversive stressful state. One striking signature of GRPR itch neurons is a short-term suppression of the firing rate (from ~2 to ~1 Hz) immediately preceding the look onset. It is possible that this may reflect intrinsic constraints on the spiking generating synaptic machinery of GRPR itch neurons, which could necessitate the suppression to lower the threshold for them to fire action potentials more readily upon receiving itch inputs. In support of this, activation of GRPR itch neurons, a process exclusively mediated by GRP (Yu et al., 2017), is of slow kinetics typical of neuropeptide-mediated GPCR activation (Chen, 2021), and may also be limited by the amount of GRP available. Interestingly, early studies reported similar suppression (Kuffler and Eyzaguirre, 1955; Perkel and Mulloney, 1974; Perkel et al., 1964). For example, paradoxical inhibition of firing rates is considered to be necessary for facilitating the localization of the source of sound in the auditory system (Cook et al., 2003; Dodla and Rinzel, 2006). It will be interesting to determine whether the suppression may result from scratching motion-elicited attention before the look onset. Moreover, our results are consistent with an underappreciated notion that SCN neurons possess the capacity to discriminate spatial pattern information (Dobb et al., 2017; Mouland et al., 2017; Stinchcombe et al., 2017).

GRPR neurons transmit visual itch and stress information via parallel pathways

Our studies identify the retina-ipRGCs-SCN-PVT pathway as a non-canonical visual pathway for relaying contagious itch information. Interestingly, the PVT could relay sensory-related information to higher cortical areas, and plays a role in awareness and anticipatory behavior in response to stressful situation in a circadian-independent manner (Kirouac, 2015; Van der Werf et al., 2002). Given that contagious itch is a multifaceted socio-psychological stimulus, different features of visual itch information could be relayed through distinct subcortical neural pathways. It is possible that PVT GRPR neurons may monitor and convey salient itch information that encodes negative valence and salience of arousal (Kirouac, 2015).

The identification of the retina-ipRGCs-SCN-PVN pathway confers CIB with evolutionary and ethological significance. The SCN could regulate corticosterone release in the PVN in a circadian-dependent manner (Jones et al., 2021; Koch et al., 2017; Ulrich-Lai and Herman, 2009). The prominent innervation of the PVN by GRPR neurons suggests that the SCN GRPR neurons might mediate social stress transmission by activating the SCN-PVN pathway and the HPA axis (Figure 8). To date, only limited evidence has implicated SCN in circadian-independent stress regulation (Buijs et al., 1993, 1999; Kalsbeek et al., 1996).

Our studies provide crucial evidence that SCN could regulate circadian- and melanopsin-independent visual and psychological stress responses. The PVN could be a convergent node for regulating both cutaneous and contagious itch-induced stress/anxiety-like responses (Chen, 2021; Misery et al., 2018).

The striking observation that CIB arises independently of the visual cortex is supported by the finding that SCN GRPR neurons coordinate different aspects of CIB through several subcortical pathways. How do mice without the visual cortex recognize the complex scratching behavior of conspecifics? In fact, primary visual cortex-independent visual behaviors, such as pattern discrimination, are well documented in a variety of animal species, from humans and nonhuman primates (Leopold, 2012; Weiskrantz, 2009) to mice (Prusky and Douglas, 2004), rats (Dean, 1981), cats (Winans, 1967), hamsters (Schneider, 1969), and gerbils (Ingle, 1981). Both lower vertebrates and invertebrates are capable of complex motion vision (Prete, 2004). Classic studies also showed that frogs lacking a definite visual cortex do not respond to stationary prey but nonetheless can snap the prey according to its stereotyped moving patterns (Ingle, 1968; Lettvin et al., 1959). In this context, we postulate that the emergence of the retina-ipRGCs-SCN-PVN/PVT ancestral pathway may arguably predate the neocortex (Menaker et al., 1997; Rakic, 2009) and may have contributed to subcortical circuits that detect ethologically relevant motion stimuli in some of the aforementioned studies. Conceivably, primitive mammals living in an ecological niche, likely being replete with mosquitoes/parasites, might necessitate the visual detection and instinctive copy of the scratching motion of conspecifics. Such visual behavior might afford a competitive edge for the survival of conspecifics by anticipating and adapting to impending challenging conditions absent direct visual contact with stimuli, which could fall short of observable visual space. Because of its value for survival, the scratching motion as a whole must be familiar and recognizable to the retina of observing conspecifics. Nonetheless, the precise mechanisms by which the retina photo-receptors encode scratching motion awaits further studies.

Contagious itch: A primitive form of emotional contagion

The present study may help us to understand the origin of emotional contagion. At first glance, CIB can be viewed as a form of instinctive motor mimicry that is ubiquitous across lower vertebrates and invertebrates (e.g., fish schools, bird flocks, etc.) (Chartrand and Lakin, 2013). Unlike contagious pain and some emotional contagions in rodents that are socially transmissible only between familiar conspecifics (Chen, 2018; Kim et al., 2019; Langford et al., 2006), familiarity is not a prerequisite for social transmission of itch. Thus, itch contagion appears to be more primitive and likely evolved earlier than those emotional contagions found only between familiar conspecifics (de Waal and Preston, 2017). On the other hand, the observation that the scratching motion encodes salient stressful cues not only implies its ancestral roots of origin but further argues that CIB is an emotional contagion rather than motor mimicry. Phylogenetically, contagious itch might have evolved more recently than motor mimicry.

In summary, our studies identify ipRGCs as an upstream and PVT as a downstream station of SCN GRP and GRPR neurons for relaying contagious itch. We show that the retina-

ipRGCs-SCN-PVT pathway is a non-canonical subcortical visual pathway that is necessary and sufficient for mediating CIB in a melanopsin-independent manner. Our finding also suggests that GRPR neurons project to the PVN to mediate stress response. The correlation between the neural dynamics of GRPR itch neurons and scratching motion strengthens the notion that SCN GRPR neurons are a vital visual circuit. Whether the retina-ipRGCs-SCN visual pathway may transmit additional naturalistic fast-moving stimuli that encode stressful information merits further research.

Limitations of the study

There are several limitations of the study. First, the readout of CIB is very small. On average, only a few imitative scratches can be detected during 30 min CIB test. The look behavior is subjective since we cannot be certain whether observer mice gaze on the screen or the “look” behavior is merely co-incidental with the head movement. Second, slow-acting GRP-mediated weak activation of GRPR itch neurons makes the isolation of itch-induced response from baseline neural dynamics and firing rates technically difficult. Finally, the deeply embedded small SCN (~300 μm diameter) in the basal hypothalamus located at the base of the brain has also made it challenging to interrogate the neural activity of GRPR neurons in freely behaving mice using either *in vivo* microendoscopic calcium imaging with GRIN lens (~500 μm diameter) or multichannel extracellular recording with the electrode (~250 μm diameter) in real time.

STAR★METHODS

RESOURCE AVAILABILITY

Lead contact—Further information and requests for resources and reagents should be directed to and will befulfilled by the lead contact Zhou-Feng Chen (chenz@wustl.edu).

Materials availability—No reagents were generated in the study.

Data and code availability

- All data reported in this paper will be shared by the lead contact upon request.
- All custom code used in this study are available from the lead contact upon reasonable request. *Optogenetic tagging* SALT Matlab code (Kvitsiani et al., 2013) is available at http://kepecslab.cshl.edu/salt.m.
- Any additional information required to reanalyze the data reported in this paper available from the lead contact upon request.

EXPERIMENTAL MODEL AND SUBJECT DETAILS

Adult male C57BL/6J (Jackson Laboratory), *Grpr*^{iCre} (Munanairi et al., 2018), Ai32 or Ai9 (Madisen et al., 2012), *Opn4* KO (Lucas et al., 2003), *Opn4*^{Cre} (RRID: MMRRC_036544-UCD), *Tra2β* CKO (Diao et al., 2018), *Adcyap1*$^{f/f}$ (Ross et al., 2018), *Grp*^{Cre} (Yu et al., 2017), *Adcyap1*^{Cre} (Tan et al., 2016) and their respective WT littermates were used in this study. Mice were housed in clear plastic home cages with no more than 5 mice per cage in a controlled environment at a constant temperature of 23°C and humidity of 50 ± 10% with

food and water available *ad libitum*. The animal room was on a 12/12 h light/dark cycle with lights on at 6 am. Male mice at age of 7 to 12 weeks old were used for experiments. Age-matched animals were used randomly for each group in each experiment. All behavioral experiments were performed in accordance with the guidelines of the National Institutes of Health and were approved by the Animal Studies Committee at Washington University School of Medicine.

METHOD DETAILS

Drugs and virus—Clozapine ($C_{18}H_{19}ClN_4$, Sigma-Aldrich) was i.p. injected at 0.1 mg/kg for chemogenetic inhibition 30 min before test. CRF1 receptor antagonist CP154,526 ($C_{23}H_{32}N_4 \cdot HCl$, Sigma-Aldrich) was i.p. injected 30 min at 10 mg/kg before the CIB test. AAV5-EF1α-DIO-ChR2-(H134R)-eYFP (2.5×10^{12} mL), control virus AAV5-EF1a-DIO-eYFP/mL), AAV8-hSyn-DIO-h4MDi-mCherry (2.7×10^{12} vg/mL), AAV2-Syn-Cre-IRES-GFP (6.3×10^{11} vg/mL), control virus AAV5-EF1α-DIO-eYFP (1.9×10^{13} vg/mL) were provided by Hope Center Viral Vectors Core, Washington University St. Louis. The following viruses were used: AAVDJ-EF1α-DIO-GCaMP6s (Stanford Viral Vector Core. RetroAAV-Ef1α-mCherry-IRES-Cre, 1.3×10^{13} vg/mL), AAV5-hSyn-DIO-HA-hM4D(Gi)-IRES-mCitrine (6.6×10^{12} vg/mL), AAV5-hSyn-eGFP-Cre-WPRE (1×10^{13} vg/mL), control virus AAV5-hSyn-DIO-mCherry (1.1×10^{13} vg/mL, Addgene). AAV8-Ef1α-DIO-RVG-WPRE-hGH-pA (>2×10^{12} vg/mL), AAV8-Ef1α-DIO-H2B-EGFP-T2A-TVA-WPRE-hGH-pA (2×10^{12} vg/mL), RV-ENVA-ΔG-dsRed (2×10^{12} vg/mL, BrianVTA). RVG-9R protein (Kumar et al., 2007) (YTIWMPENPRPGTPCDIFTNSRGKRASNGGGGRRRRRRRRR, Bachem). *Adcyap1r1* siRNA was purchased from Sigma (NM_001025372).

Behavior

Contagious itch behavior test: Contagious itch behavior (CIB) tests were performed as previously described (Yu et al., 2017). Briefly, a video clip on a computer LED screen (1028 × 736 resolution) showing the mouse demonstrator scratching the nape continuously for 1 h at a constant speed (60 scratches/min) or 1 Hz. A video clip (30-s loop for 1 h) showing a mouse that ambulates without scratching behaviors was used as a control. A mouse scratch is defined as a lifting of the hind limb on the skin and then a replacing of the limb back to the floor, regardless of how many scratching strokes between these two movements. The observer was placed in a clear plexiglass cylinder (10.79 cm × 17.78 cm) next to the computer LED screen and allowed to acclimate for 10 min. The demonstrator in the video was adjusted to the same size and aligned to the same level of a mouse observer. The observing mice were recorded for 1 h and their behaviors were counted by the person blinded to the group or genotype of the mice. CIB was recorded between 7–11 am. A look behavior was defined as a pause and look (~1 s) towards the screen. It should be noted that the look described here differs from the gaze used in the visual field since we were unable to differentiate between a random head movement towards the computer screen and a gaze selectively tuned to the motion displayed on the screen. A vast majority of look behaviors were related to random head movement. An imitative scratch ('look-and-scratch') is defined as the scratch occurring within 5 s following a look behavior ('look-and-scratch'). Note that a few seemingly "look-and-scratch" behaviors were detected in control mice, which can be

attributed to the fact that look behavior may coincide with spontaneous scratching behavior. Animal behaviors were videotaped (SONY HDR-CX190) from a side angle and played back on the computer for assessments by the observer blinded to the treatments and the genotypes of animals.

Open field test—The open field test apparatus consists of a square box (30 cm × 30 cm × 30 cm), placed in a cabinet with white noise, and infrared light. A camera was placed above the box and connected with the Any-maze tracking system (version 6.22; Stoelting CO, IL). The box was divided into 16 equal squares. The 12 squares adjacent to the wall are considered “peripheral”, whereas the 4 squares in the middle of the floor are considered “central”. Animals were acclimated to the testing room for at least 30 min prior to the CIB test. After the CIB test, mice were placed in the open field box for 30 min to allow for free movement and exploration. Mice behavior was analyzed by Any-maze software.

Light-dark box test—The light-dark box test apparatus was modified according to a previous study (Takao and Miyakawa, 2006). Briefly, it consists of a dark and a light rectangular compartment (60 cm × 30 cm × 30 cm), placed in a test chamber. The box was partitioned into two compartments with an opening between them. Only the top of the dark compartment was covered with black plastic. A camera was placed above the box and connected with the Any-maze tracking system (version 6.22; Stoelting CO, IL). Prior to the CIB test, mice were acclimated to the testing room for at least 30 min. After the CIB test, each mouse was placed in the light box for 10 min. The distance each mouse traveled and time spent in each compartment were analyzed by Any-maze software. All tests were conducted between 8 am - 12 pm.

Visual cliff test—A modification of the visual cliff was employed (Mazziotti et al., 2017). Visual cliff was tested in an open-topped plexiglass box (50 cm × 30 cm × 23 cm). The box was positioned on the edge of a bench so that half of the base covered the bench (shallow side) while the other half was suspended over the edge of the bench 90 cm above the floor (cliff side), creating the appearance of a cliff without an actual drop-off. A LED monitor with a checkerboard pattern (2.5 cm × 2.5 cm) was placed under the bench side of the box as well as on the floor underneath the box to emphasize the cliff drop-off. The brightness and contrast of the two monitors were set to be identical. The room was kept in the dark with a black curtain to separate the set-up to avoid distractions. Individual mice were placed in the middle of the box at the edge of the cliff facing the cliff side. The behavior of mice was recorded for 10 min. The total time that mice spent on the cliff or the shallow side was counted by the observer blinded to the experimental designs.

Sweeping test—The sweeping test was performed as described previously (De Franceschi et al., 2016). Briefly, each mouse was placed in a closed plexiglass box (50 cm × 30 cm × 23 cm) with an LED monitor on the top and allowed to freely explore the box for 15 min prior to the sweeping test. The sweeping stimulus was a black dot (5 cm diameter) that was shown to be moving from one corner of the LED screen in a straight diagonal path (total length: 59 cm) 2 times within 30 s for 5 min. The behavior of each mouse was recorded

using a camera. The total freezing time of mice was counted by observers blinded to the experimental designs.

Hot plate test—Stress-induced analgesia effect was measured using the hot plate test as described previously (Sun et al., 2009). Prior to the CIB test, animals were acclimated to the testing room for at least 30 min. After the CIB test, the latency for the mouse to lick its hind paw or jump was recorded with a 30 s cutoff.

Immunohistochemistry (IHC)—IHC was performed as previously described (Yu et al., 2017). Mice were anesthetized (ketamine, 100 mg/kg and xylazine, 15 mg/kg) and perfused intracardially with PBS pH 7.4, followed by 4% paraformaldehyde (PFA) in PBS. Tissues were dissected, postfixed in 4% PFA for 8 h, and cryoprotected in 20% sucrose in PBS overnight at 4°C. For histology of mice with GRIN lens and optrode in SCN, the whole brain with the lens in position was postfixed for 3 days, followed by the removal of lens/optrode and brain dissection. For immunostaining of whole-mount retinas, the cornea, lens, and vitreous body were removed. The retinas were carefully quartered into a 4-"pedaled", flower-like structure under the dissecting scope. Brain tissues were sectioned at 30 μm thickness in optimal cutting temperature (OCT) using a cryostat microtome. Sections or whole retina were then washed three times with PBS and blocked in 2% donkey serum and 0.3% Triton X-100, followed by incubation with primary antibodies overnight at 4°C and washed three times with PBS. Secondary antibodies were incubated for 2 h at room temperature and washed three times with PBS. Sections or whole retinas were mounted on slides, and ~100 μL FluoromountG (Southern Biotech) was placed on the slide with a coverslip.

The primary antibodies used were rabbit anti-melanopsin (1:2000, Advanced Targeting Systems, AB-N38), rabbit anti-GRP (1:500, Immunostar, 20073), chicken anti-GFP (1:400, Aves Labs, GFP-1020), and mouse anti-mCherry (1:1000, Developmental Studies Hybridoma Bank, 3A11). Guinea Pig anti-RBMPS (1:1000, PhosphoSolutions, 1832-RBPMS), rabbit anti-PKCα (1:1000, Santa Cruz), rabbit anti-GRPR (1:800, MBL), and rabbit anti-PKCβ (1:1000, Santa Cruz), rabbit anti-AVP (1:1000, Immunostar) rabbit anti-VIP (1:1000, Immunostar). The secondary antibodies were CY3-conjugated donkey anti-rabbit (1:500, Jackson Immuno-Research, 711-165-152), CY3-conjugated donkey anti-mouse (1:500, Jackson Immuno-Research, 715-165-150), and Alexa Fluor® AffiniPure donkey anti-chicken (1:500, Jackson Immuno-Research, AB_2340375). Fluorescent Images were taken using a Nikon C2+ confocal microscope system (Nikon Instruments, Inc.). For whole-brain mapping, images were taken using the Hamamatsu NanoZoomer 2.0-HT System and NDP. View for image viewing. Analysis of images was performed using ImageJ software (Schindelin et al., 2012). For each treatment group, three sections were averaged in each mouse, and 3~6 mice were used for statistical analysis. Immunoreactive cell numbers were counted in the whole mounted retina. Immunoreactive cell numbers or fluorescent intensity in the entire SCN were analyzed.

RNAscope® *in situ* hybridization (ISH)—A high amplification system for the detection of single-molecule RNA fluorescence *in situ* hybridization, RNAscope® (Advanced Cell Diagnostics (ACD), Hayward, CA), was used for verification of *iCre* mRNA

expression in the SCN and PVT of *Grpr*^{iCre} mice, *Adcyap1r1* expression of *Grpr*^{iCre} mice and the co-localization of *Adcyap1r1* and *Grp* in SCN. The tissue preparation procedure was the same as described above for the IHC experiments. Brain tissues were sectioned at 20 μm thickness in OCT using a cryostat microtome and mounted directly on SuperFrost Plus slides (Thermo Fisher Scientific, Waltham, MA). RNAscope experiment was performed according to our previous studies (Munanairi et al., 2018). Mouse-specific probes for *Grpr* (317871-C2, ACD) and *iCre* (423321-C3, ACD) *Adcyap1r1* (409561-C1, ACD), and *Grp* (317861-C2, ACD) were purchased from Advanced Cell Diagnostics. Fluorescent Images were taken using a Nikon C2+ confocal microscope system (Nikon Instruments, Inc.) and analysis of images was performed using ImageJ software from NIH Image (version 1.34e). For each group of treatment, three sections were averaged in each mouse, and 3~6 mice were used for statistical analysis. Cell numbers in the entire SCN were counted.

ELISA assay—Corticosterone level in the blood serum was assayed using the Corticosterone ELISA kit according to the product protocol. Briefly, after the CIB test, mice were anesthetized using isoflurane. Blood was collected by a needle punch in the submandibular vein (cheek punch) (Golde et al., 2005) into a blood collection tube (Thermo Fisher Scientific), and centrifuged for 10 min at 10000 rpm. Serum was collected and subjected to the ELISA assay or stored at −80°C for future assay.

Intravitreal injections—Intravitreal injections were performed using insulin syringes (0.3cc, 30 gauge, Exelint) on 6-week-old mice under anesthesia with ketamine (100 mg/kg, i.p.) and xylazine (10 mg/kg, i.p.). Mice were placed on their side with one eye facing up. Eyelids were gently retracted, allowing the eyeball to protrude. The needle was gently inserted into the sclera for 2 mm and 3 μL of the solutions were slowly injected and then quickly pulled out to minimize reflux and allow self-sealing of the scleral tunnel. Melanopsin-saporin (400 ng, Advanced Targeting Systems, IT-44), control-saporin (400 ng, Advanced Targeting Systems, IT-21), AAV8-hSyn-DIO-h4MDi-mCherry, or control virus (AAV5-EF1α-DIO-eYFP) (Hope Center Viral Vectors Core, Washington University St. Louis) was injected bilaterally. AAV5-EF1α-DIO-ChR2-(H134R)-eYFP or control virus were injected unilaterally into the right eye. Mice with saporin and virus injections were allowed to recover for 2 and 3 weeks, respectively, prior to behavioral and IHC experiments.

Brain lesion—Mice were anesthetized with ketamine (100 mg/kg) and xylazine (10 mg/kg) and fixed on a stereotaxic apparatus (Stoelting) 1 h after subcutaneous administration of Buprenorphine SR (0.5 mg/kg) subcutaneous administration for analgesia. Ophthalmic ointment was dabbed on the eyes to protect them from drying. The occipital skull was drilled to expose the visual cortex. Visual cortical areas on both hemispheres, including Brodmann areas 17, 18a, and 18b were removed by aspiration (Kaneda et al., 2012). For the superior colliculus (SC) lesion, the skull overlying the colliculus was incised, and the SC area on both hemispheres were removed by aspiration (Kaneda et al., 2012). Following the brain lesions, the empty space was filled with sterile gel foam. Mice with sham surgery were treated as above up to the point of aspiration of the visual cortex. Mice were given 2 weeks for recovery.

Intracranial injections—Stereotaxic surgery was performed as previously reported (Yu et al., 2017). Briefly, mice were anesthetized (ketamine, 100 mg/kg and xylazine, 15 mg/kg, i.p.) and fixed on a stereotaxic apparatus (Stoelting). Prior to surgery, mice were administered with Buprenorphine SR for analgesia. Mouse eyes were protected with ophthalmic ointment. A small hole was drilled through the skull with a dental drill (0.8 mm bit). RetroAAV-Ef1a-mCherry-IRES-Cre virus was injected bilaterally in the SCN of C57BL/6J mice (Bregma: A-P −0.43 mm; M-L ± 0.15 mm; DV −6.0 mm) using a QSI automatic injector (Stoelting) at a rate of 40 nL/min through a 1-μL Hamilton Neurosyringe with a 30-gauge beveled needle. The injection needle was withdrawn 5 min after injection. Mice with virus injection were allowed to recover for 3–4 weeks prior to the second virus injection, behavior or IHC experiments. For monosynaptic tracing, a mix of helper virus AAV2/9-Ef1α-DIO-RVG-WPRE-pA and AAV2/9-Ef1α-DIO-His-EGFP-2a-TVA-WPRE-pA was injected into SCN. 3 weeks later, RV-ENVA-ΔG-dsRed was injected into SCN. Mice were perfused for IHC 10 days later. For neuron ablation, Bombesinsaporin (BB-sap) (40 ng/200 nL, Advanced Targeting Systems, IT-40), PACAP-saporin (20 ng/200 nL, Advanced Targeting Systems, IT-84) or Blank-sap was injected into bilateral SCN. For RVG-9R mediated knockdown, RVG-9R protein was dissolved with 10% glucose at 1.45 μg/μL, and then mixed with the same volume of 2 μg/μL *Adcyap1r1* siRNA. The mix was then injected into bilateral SCN (200 nL for each side) after 15 min at room temperature. Behaviors or IHC were performed from day 6 to day 7 after injection.

Optogenetic stimulation—Three weeks after intravitreal virus injection, a custom-made ferrule with fiber-optic (200 μm in core diameter, Doric Lenses) was placed in the SCN shell, dLGN, SC, and fixed on the skull with anchor screws (Harvard Apparatus, CMA7431021, Holliston, MA), super glue gel (Kwik-Fix, 1705007535, Elburn, IL) and dental cement (Lang Dental, Wheeling, IL). The optical stimulation was performed as previously described (Yu et al., 2017), using the following stereotaxic coordinate: SCN, anterior-posterior (A-P) −0.43 mm, medial-lateral (M-L) −0.15 mm, dorsal-ventral (D-V) −6.00 mm from Bregma; dLGN, A-P −2.46 mm, M-L 2.20 mm, D-V −3.22 mm from Bregma; SC, A-P −3.80 mm, M-L 0.65 mm, D-V −1.10 from bregma. For photo-stimulation, mice in a home cage were photo-stimulated by attaching the ferrule to a fiber optic cable with a rotary joint (Doric lenses, Quebec, Canada), followed by another fiber optic cable that was attached to a fiber-coupled 473 nm blue laser (BL473T8-150FC, Shanghai Laser and Optics Co.) with an ADR-800A adjustable power supply. Mice were subject to a total of 5 trains of stimulation (1, 5, 10, 20, or 30 Hz with 10 ms on-pulse, 10 mW power from fiber tip) for 2 min with 10 min intervals. Laser power output from the fiber optic was measured using a photometer (Thor Labs, Newton, NJ). An Arduino UNO Rev 3 circuit board (Arduino) was programmed and attached to the laser via a BNC input to control the frequency and timing of the stimulation. Mouse behavior was recorded and counted by observers blinded to the animal groups.

Slice electrophysiology—The brain of *Grp*^{Cre}; *Ai9* mice (2–3 weeks old) was isolated under oxygenated (95% O_2, 5% CO_2) sucrose-based dissection solution (in mM, 209 Sucrose, 2 KCl, 1.25 NaH_2PO_4, 5 $MgCl_2$, 0.5 $CaCl_2$, 26 $NaHCO_3$, 10 Dextrose, pH was adjusted to 7.3~7.4). Sections of the SCN were obtained at 300 μm using a vibrating slicer

(Vibratome 1000plus). Slices were recovered in a chamber containing 37°C oxygenated ACSF (in mM, 124 NaCl, 2.5 KCl, 1.25 NaH_2PO_4, 24 $NaHCO_3$, 5 HEPES, 12.5 Dextrose, 1 $MgCl_2$, 2 $CaCl_2$, pH was adjusted to 7.3 7.4) for at least 1 h.

Grp^{tdTom} neurons were visualized with 593 nm light (TXRED filter) under an upright microscope (Olympus BX 51WI). Slices were mounted in a chamber (Warner RC 26G) and perfused with oxygenated ACSF at 2 mL/min. Patch pipettes were pulled to resistance of 6–8MΩ. Signals were amplified with Multiclamp 700B and Digidata 1550A, and pClamp 10.7 software. Signals were filtered at 2 kHz and digitized at 10k Hz. Glutamate (500 μM) was applied for 90 s to induce an inward current. After 5 min wash with ACSF, slices were incubated with 200nM PACAP for 3 min, then glutamate was applied for another 90s for recording at −60mV. Recorded *Grp*^{tdTom} neurons were collected for single-cell PCR (Single Cell-to-CT™ qRT-PCR Kit, Invitrogen) for confirmation. Data were analyzed with Clampfit 10.7, Minianalysis (Synaptosoft), and GraphPad Prism 7 software. Traces were plotted using Origin 2015 software.

***In vivo* Ca^{2+} imaging—**Intracranial virus injection was performed using *Grpr*^{iCre} mice (male 25–28 g) followed by lens implant surgery. Briefly, *Grpr*^{iCre} mice were anesthetized using isoflurane (4~5% for induction, 2~3% maintenance in oxygen 1 h after subcutaneous administration of Buprenorphine SR (0.5 mg/kg) subcutaneous administration for analgesia. Five or six anchor screws were implanted on the skull to help stabilize the lens. A round craniotomy (~1 mm diameter) was made on the skull and 0.2 μL AAVDJ-EF1α-DIO-GCaMP6s (Stanford Viral Vector Core) were unilaterally injected into the left side of the SCN using a 10° angled stereotaxic coordinates (Bregma: AP −0.43 mm; ML −1.12 mm; DV − 6.09 mm). A virus dilution study was performed in advance to ensure an appropriate expression level of GCaMP6s in GRPR neurons, which enabled the indication of Ca^{2+} dynamic during the behavior study period. To determine the optimal concentration for GCaMP6s expression with minimal toxicity, the virus was serially diluted with saline (1:1, 1:4, 1:6, 1:8, 1:10, n = 4 mice for each) and tested *in vivo*. A 1:6 dilution was eventually chosen to ensure that healthy expression of GCaMP6s for calcium imaging of GRPR neurons over the period of 2 months post viral injection (Zariwala et al., 2012). After removing the Neurosyringe, a gradient refractive index (GRIN) lens was slowly lowered into the brain (10 μm at a time/ every other 6 s) until the bottom of the lens was situated about 200 μm above the injection site. Kwik-Sil (World Precision Instruments, Sarasota, FL) was used to fill the space between the brain tissue and the lens to protect the exposed brain tissue. Metabond (Parkell, Inc. Edgewood, NY) was used to permanently fix the lens to the surrounding skull and the screws. The top of the lens was protected with a parafilm and Kwik-Sil. A head ring was placed on the skull surrounding the lens with Metabond. Mice were placed in a single-housed home cage with hydrogel and food to protect mice from damaging the lens.

Two weeks after the lens implantation, a magnetic baseplate (Inscopix, Palo Alto, CA) was installed on the animal to allow a firm miniscopic connection and to ensure a stable view of cells over multiple days. Briefly, the animal was head-fixed on a customized stage, and the miniature microscope (nVista HD, Inscopix, Palo Alto, CA) was mounted to the baseplate by a screw and attached to the stereotaxic arm. After setting the miniscope objective parallel

to the top of the lens, the miniscope was lowered down until a sharp image was obtained from the back of the focal plane with an integrated LED (473 nm) power on. Adjust the z arm of the stereotaxic until the best focal plane was found with the largest number of dynamic neurons with the nVista HD Acquisition Software (v2.0.4, Inscopix). Then the baseplate was fixed with Metabond in position on the animal head such that Metabond did not get into the gap between the objective and lens. 20 min later, the miniscope was removed from the baseplate freely and a baseplate cover (Inscopix, Palo Alto, CA) was placed on the baseplate. Then the animal was returned to the home cage. A dummy miniscope was used for mice to get used to the weight of the miniscope while freely moving in the cage 30 min/day for 3 days.

Before the experiment, the miniature microscope was connected to the magnetic baseplate and secured with a screw. The mouse was returned to its home cage for 10 min for acclimating to the miniscope and then placed in the cylinder next to a LED screen for the CIB test. A mouse scratching or ambulating video was played on the LED screen for 30 min. CIB was recorded between 9–12 am using the Any-Maze recording system (version 6.22; Stoelting CO, IL) while Ca^{2+} imaging recording by the nVista HD Acquisition Software was triggered by the Any-Maze recording system using a transistor-transistor logic (TTL) connection, so that the Ca^{2+} data was synchronized with the behavioral data. In the meantime, a demo video was recorded using a CANON camera and focused on the observer mouse from a different side view. Imaging acquisition was set at 10 frames per second with a range of 30–40% of the LED intensity, Gain at 2–4. A total of 8 mice were successfully imaged and recorded for the CIB test. An average of 3 ~ 4 imitative scratches were identified for each mouse. Since the imitative behaviors of these mice happened mostly before 4 s following the look behavior, the −4 ~ 0 s and 0 ~ 4s Ca^{2+} data were used for comparison.

The recording images were processed using the Inscopix Data processing Software (version 1.3.0.2723; Inscopix, Palo Alto, CA) and analyzed with custom MATLAB code. Briefly, a spatial down-sampling of 2× of the preprocessing algorithm was applied to each video sequence to reduce the large file size and decrease the processing time. A spatial filter algorithm was applied to remove low and high spatial frequency content from microscope movies. Each video sequence was subjected to the Motion Correction algorithm according to the mean image to correct for the brain movement. The ΔF/F algorithm was used to generate the ΔF/F trace and remove any remaining spatial variation in the intensity of the signal. Neurons were defined by manually selecting ΔF/F graphs of the field of view. Auto Accept/Reject Cells tool is used to automatically classify cell statuses based on images and trace metrics. The default criteria are 1) 7 pixels < cell size <70 pixels, 2) signal to noise ratio >2, and 3) event rate >0.001 Hz. An event detection algorithm was applied to define Ca^{2+} transients, which automatically identify when bursts of cell activity occur in cell sets. For each neuron across all trials, ΔF/F between −10 s and 10 s of a specific event were extracted. The behaviors within 10 s following another behavior (look) were excluded to avoid interference. Each extracted trace after-stimulus was normalized to the pre-stimulus baseline window. Cells were classified as being excited (activated response) or inhibited (inhibited response) by a behavior event (look) if there is a significant increase or decrease between the average activity 4 s before and 4 s after the behavior event by a paired *t* test.

In vivo multichannel extracellular recording

Optrode implantation: The optrodes (optical-electrode) were self-made by combining 8 tetrodes twisted from polyimide-insulated tungsten wires (diameter, 20.3 μm; California Fine Wire Company) together with an optical fiber (200 μm in core diameter, Doric Lenses) and a self-made microdrive that enables the movement of the optrode in the D-V direction after surgery by turning the screw (diameter = 1.1 mm, thread = 250 μm). One full turn of the screw would move the microdrive for 250 μm. As described previously (Ma et al., 2019), two printed circuit boards (PCB) and one flexible printed circuit (FPC) cable were used to connect the electrode with the pre-amplifier in order to release the mechanic force of the pre-amplifier connection to the 3D-printed protective hat other than the drive itself. The tetrode wires were connected to the PCB with gold pins (Neuralynx). *Grpr*^{iCre}:*Ai32* mice (n = 13) were anesthetized with isoflurane (4% for induction, 2–3% maintenance in oxygen). The 32-channel optrode was implanted 300 μm above the left side of the SCN (AP, −0.43 mm; ML, 0.15 mm; DV, −5.60 mm). The space between the brain tissue and the optrode was filled with a 1:1 mixture of paraffin oil and paraffin (58°C melting point) (Millipore Sigma, St. Louis, MO) to protect the exposed brain tissue and enable the movement of the optrode after surgery. Metabond (Parkell, Inc. Edgewood, NY) was used to permanently fix the optrode base to the surrounding skull with six anchor screws. One stainless screw was tapped into the skull post lambda for stabilization, while the other served as ground and reference site. A 3D-printed protective hat was fixed on the skull to protect the electrode and absorb external forces. The 3D model was designed in 123D-Design (Autodesk Inc.). The hat was wrapped with copper tape and connected with the system ground to gain extra protection against electrical noises. After surgery, mice were single-housed with hydrogel and food provided on the cage floor to protect the optrode. One week later, the optrode was gradually lowered through the microdrive (≤70 μm/day) until it reached the SCN. The position of the tips was optimized at the end of each daily session to obtain the maximal unit yield.

Extracellular recording during CIB: Mice were habituated in the home cage for 1 h with the electrodes and optical fiber connected to the recording system and the laser stimulation system (BL473T8-150FC, Shanghai Laser and Optics Co.), respectively. Blue light pulses (1 – 20 Hz, 1 ms, 1–4 mW) were delivered to the SCN for 5 min to identify GRPR neurons. The mouse with optrode was placed in the cylinder next to a LED screen for the CIB test as described above. Mouse behaviors were recorded at a frame-synchronized mode by a Basler acA1920-40gc camera (Basler AG, Ahrensburg, Germany). Electrophysiological data were recorded using an Intan RHD2000 system (Intan Technologies) sampled at a 20 kHz rate. With heavy optical fiber and electrode on the head, the observers were much less mobile and consequently displayed approximately only 25 looks per recording, significantly fewer than naïve mice without the optical fibers and electrode implanted (about 40 looks). Accordingly, the average number of look-and-scratch per recording is about 2 (approximately 8% of look behavior). Of 13 mice implanted and recorded, only 7 displayed CIB with the electrode implanted above the SCN accurately. The recording was typically conducted between 9–11 am and a total of 18 recordings were obtained from 7 mice for data analysis.

Spike sorting: Spikes were isolated offline and sorted into single units by using high-dimensional cluster analysis with the masked EM algorithm for Gaussians mixtures implemented in *KlustaKwik* (Kadir et al., 2014). Electrophysiological data were visualized in Neuroscope and Klusters (Hazan et al., 2006). Manual curation was made to all automatic clustered units. All the automatic clustered units were carefully inspected by the autocorrelogram (ACG) and crosscorrelogram to remove noise clusters and merge clusters belonging to the same unit. Only well-isolated units (amplitude >50 mV; L-ratio < 0.05; ISI index <0.2); overall firing rate >0.05 Hz was considered as a single unit signal. The peri-event histogram (PETH) of GRPR neuron firing rate was obtained for further statistical analysis.

Optogenetic tagging of GRPR neurons: Blue light pulses (20 Hz, 1 ms, 1–4 mW) were delivered to the SCN for 5 min to identify GRPR neurons. The laser was triggered through an Arduino UNO Rev 3 circuit board (Arduino) controlled by custom-built MATLAB programs (MathWorks). The trigger TTL pulses were also recorded by the data acquisition system for synchronization. Stimulus-Associated spike Latency Test (SALT) was employed to determine if single laser pulses significantly modulated a single-unit activity (SUA) by comparing the first-spike latency following single laser pulses to that in arbitrary moments without a laser presentation (Eshel et al., 2015; Kvitsiani et al., 2013; Tian and Uchida, 2015). The method was described in detail previously (Kvitsiani et al., 2013) and the Matlab code is available at http://kepecslab.cshl.edu/salt.m. A single unit was identified as a GRPR neuron if the spike timing was significantly changed by blue light pulses ($p < 0.01$).

Data analysis: The firing rates of GRPR neurons between −5 s and 5 s were analyzed with the onset of look set at 0 s to ascertain whether there is a correlation between neuronal responses of SCN GRPR neurons and the look behavior during the CIB test. For each neuron, PETHs aligned to the onset of individual look behaviors were calculated in a 100-ms bin, and the firing rate of each neuron was normalized to the baseline (5 s before the look) using Z-score and smoothed by a window of 500 ms (five bins). Due to the low firing rates of GRPR neurons, an analysis based on the 2-fold change yielded few neurons with a significantly excitatory response. To avoid the underestimation of the number of GRPR itch neurons, we used a 1.5-fold change of the firing rate as the criterion for defining an excitatory response. Neurons with 1.5 fold-increase of the mean firing rate were classified as being activated, while those with a 1.5 fold-decrease of the mean firing rate as being inhibited. The rest were classified as non-responders. A total of 26 GRPR neurons that displayed significant excitatory responses in the imitative scratch group were classified as GRPR itch neurons, while the rest as GRPR non-itch neurons. The Z-scored firing rates (from −5 s to 5 s) of GRPR itch neurons were plotted using a heatmap with MATLAB. The traces for the mean Z-scored firing rate of GRPR itch neurons and GRPR non-itch neurons were also plotted across three behavioral conditions, respectively.

QUANTIFICATION AND STATISTICAL ANALYSIS

Statistical methods were indicated in the figure legend. All data were presented as the mean ± standard error of the mean (mean ± SEM). Statistical analyses were performed using Prism 9 (GraphPad, San Diego, CA). A Normality test was performed for the data

distribution. Data that did not pass the normality test were compared using a nonparametric test. Normally distributed data with equal variance were compared using two-sample or paired *t* tests. For multiple comparisons, analysis of variance (ANOVA), followed by multiple comparison test to determine statistical significance. The contingency Chi-square test was used for the percentage comparison. Significance levels indicated are as follows: ns, not significant, *$p < 0.05$, **$p < 0.01$, ***$p < 0.001$.

Supplementary Material

Refer to Web version on PubMed Central for supplementary material.

ACKNOWLEDGMENTS

We thank J.P. Yeager for mouse husbandry; H. Boozalis, S. Rana, and R. Cutinha for behavior counting; N. Sheng for help with the visual cliff test; J. Li of the Hope Center Viral Vectors Core for virus preparation; P. Stemkowski (Inscopix) for *in vivo* Ca^{2+} imaging technical support, A. Kravitz for helping with 3D printing, B.B. Lowell for *Adcyap1*$^{f/f}$ mice, and D. Kerschensteiner for comments on the manuscript. The project has been supported by the NIH grants 1R01AR056318-06, R01NS094344, and R01 DA037261-01A1 (to Z.-F.C).

INCLUSION AND DIVERSITY

We support inclusive, diverse, and equitable conduct of research.

REFERENCES

Abrahamson EE, and Moore RY (2001). Suprachiasmatic nucleus in the mouse: retinal innervation, intrinsic organization and efferent projections. Brain Res. 916, 172–191. [PubMed: 11597605]

Ali F, and Kwan AC (2020). Interpreting in vivo calcium signals from neuronal cell bodies, axons, and dendrites: a review. Neurophotonics 7, 011402. [PubMed: 31372367]

Barry DM, Liu XT, Liu B, Liu XY, Gao F, Zeng X, Liu J, Yang Q, Wilhelm S, Yin J, et al. (2020). Exploration of sensory and spinal neurons expressing gastrin-releasing peptide in itch and pain related behaviors. Nat. Commun. 11, 1397. [PubMed: 32170060]

Barson JR, Mack NR, and Gao WJ (2020). The paraventricular nucleus of the thalamus is an important node in the emotional processing network. Front. Behav. Neurosci. 14, 598469. [PubMed: 33192373]

Baver SB, Pickard GE, Sollars PJ, and Pickard GE (2008). Two types of melanopsin retinal ganglion cell differentially innervate the hypothalamic suprachiasmatic nucleus and the olivary pretectal nucleus. Eur. J. Neurosci. 27, 1763–1770. [PubMed: 18371076]

Berson DM, Dunn FA, and Takao M (2002). Phototransduction by retinal ganglion cells that set the circadian clock. Science 295, 1070–1073. [PubMed: 11834835]

Borst A, and Euler T (2011). Seeing things in motion: models, circuits, and mechanisms. Neuron 71, 974–994. [PubMed: 21943597]

Brown TM, Coogan AN, Cutler DJ, Hughes AT, and Piggins HD (2008). Electrophysiological actions of orexins on rat suprachiasmatic neurons in vitro. Neurosci. Lett. 448, 273–278. [PubMed: 18973790]

Buijs RM, Markman M, Nunes-Cardoso B, Hou YX, and Shinn S (1993). Projections of the suprachiasmatic nucleus to stress-related areas in the rat hypothalamus: a light and electron microscopic study. J. Comp. Neurol. 335, 42–54. [PubMed: 7691904]

Buijs RM, Wortel J, Van Heerikhuize JJ, Feenstra MG, Ter Horst GJ, Romijn HJ, and Kalsbeek A (1999). Anatomical and functional demonstration of a multisynaptic suprachiasmatic nucleus adrenal (cortex) pathway. Eur. J. Neurosci. 11, 1535–1544. [PubMed: 10215906]

Butler RK, and Finn DP (2009). Stress-induced analgesia. Prog. Neurobiol. 88, 184–202. [PubMed: 19393288]

Chakraborty M, and Jarvis ED (2015). Brain evolution by brain pathway duplication. Philos. Trans. R. Soc. Lond. B Biol. Sci. 370, 20150056. [PubMed: 26554045]

Chartrand TL, and Lakin JL (2013). The antecedents and consequences of human behavioral mimicry. Annu. Rev. Psychol. 64, 285–308. [PubMed: 23020640]

Chen D, Buchanan GF, Ding JM, Hannibal J, and Gillette MU (1999). Pituitary adenylyl cyclase-activating peptide: a pivotal modulator of glutamatergic regulation of the suprachiasmatic circadian clock. Proc. Natl. Acad. Sci. USA 96, 13468–13473. [PubMed: 10557344]

Chen J (2018). Empathy for distress in humans and rodents. Neurosci. Bull. 34, 216–236. [PubMed: 28493169]

Chen ZF (2021). A neuropeptide code for itch. Nat. Rev. Neurosci. 22, 758–776. [PubMed: 34663954]

Contreras E, Nobleman AP, Robinson PR, and Schmidt TM (2021). Melanopsin phototransduction: beyond canonical cascades. J. Exp. Biol. 224, jeb226522. [PubMed: 34842918]

Cook DL, Schwindt PC, Grande LA, and Spain WJ (2003). Synaptic depression in the localization of sound. Nature 421, 66–70. [PubMed: 12511955]

De Franceschi G, Vivattanasarn T, Saleem AB, and Solomon SG (2016). Vision guides selection of freeze or flight defense strategies in mice. Curr. Biol. 26, 2150–2154. [PubMed: 27498569]

de Waal FBM, and Preston SD (2017). Mammalian empathy: behavioural manifestations and neural basis. Nat. Rev. Neurosci. 18, 498–509. [PubMed: 28655877]

Dean P (1981). Grating detection and visual acuity after lesions of striate cortex in hooded rats. Exp. Brain Res. 43, 145–153. [PubMed: 7250262]

Desimone R, and Duncan J (1995). Neural mechanisms of selective visual attention. Annu. Rev. Neurosci. 18, 193–222. [PubMed: 7605061]

Diao Y, Cui L, Chen Y, Burbridge TJ, Han W, Wirth B, Sestan N, Crair MC, and Zhang J (2018). Reciprocal connections between cortex and thalamus contribute to retinal axon targeting to dorsal lateral geniculate nucleus. Cereb. Cortex 28, 1168–1182. [PubMed: 28334242]

Do MTH (2019). Melanopsin and the intrinsically photosensitive retinal ganglion cells: biophysics to behavior. Neuron 104, 205–226. [PubMed: 31647894]

Dobb R, Martial F, Elijah D, Storchi R, Brown TM, and Lucas RJ (2017). The impact of temporal modulations in irradiance under light adapted conditions on the mouse suprachiasmatic nuclei (SCN). Sci. Rep. 7, 10582. [PubMed: 28874778]

Dodla R, and Rinzel J (2006). Enhanced neuronal response induced by fast inhibition. Phys. Rev. E Stat. Nonlin. Soft Matter Phys. 73, 010903. [PubMed: 16486114]

Ecker JL, Dumitrescu ON, Wong KY, Alam NM, Chen SK, LeGates T, Renna JM, Prusky GT, Berson DM, and Hattar S (2010). Melanopsin-expressing retinal ganglion-cell photoreceptors: cellular diversity and role in pattern vision. Neuron 67, 49–60. [PubMed: 20624591]

Eshel N, Bukwich M, Rao V, Hemmelder V, Tian J, and Uchida N (2015). Arithmetic and local circuitry underlying dopamine prediction errors (vol 525, pg 243, 2015). Nature 527, 398.

Fenno LE, Mattis J, Ramakrishnan C, Hyun M, Lee SY, He M, Tucciarone J, Selimbeyoglu A, Berndt A, Grosenick L, et al. (2014). Targeting cells with single vectors using multiple-feature Boolean logic. Nat Methods 11, 763–772. [PubMed: 24908100]

Fernandez DC, Chang YT, Hattar S, and Chen SK (2016). Architecture of retinal projections to the central circadian pacemaker. Proc. Natl. Acad. Sci. USA 113, 6047–6052. [PubMed: 27162356]

Golde WT, Gollobin P, and Rodriguez LL (2005). A rapid, simple, and humane method for submandibular bleeding of mice using a lancet. Lab Anim. 34, 39–43.

Gonzales-Rojas R, Rana AN, Mason P, Renfro C, Annaluru V, Panda S, and Lee HY (2020). The mouse model of fragile X syndrome exhibits deficits in contagious itch behavior. Sci. Rep. 10, 17679. [PubMed: 33077777]

Göz D, Studholme K, Lappi DA, Rollag MD, Provencio I, and Morin LP (2008). Targeted destruction of photosensitive retinal ganglion cells with a saporin conjugate alters the effects of light on mouse circadian rhythms. PLoS One 3, e3153. [PubMed: 18773079]

Güler AD, Ecker JL, Lall GS, Haq S, Altimus CM, Liao HW, Barnard AR, Cahill H, Badea TC, Zhao H, et al. (2008). Melanopsin cells are the principal conduits for rod-cone input to non-image-forming vision. Nature 453, 102–105. [PubMed: 18432195]

Hannibal J, Ding JM, Chen D, Fahrenkrug J, Larsen PJ, Gillette MU, and Mikkelsen JD (1997). Pituitary adenylate cyclase-activating peptide (PACAP) in the retinohypothalamic tract: a potential daytime regulator of the biological clock. J. Neurosci. 17, 2637–2644. [PubMed: 9065523]

Hannibal J, Georg B, and Fahrenkrug J (2017). PAC1- and VPAC2 receptors in light regulated behavior and physiology: studies in single and double mutant mice. PLoS One 12, e0188166. [PubMed: 29155851]

Hannibal J, Møller M, Ottersen OP, and Fahrenkrug J (2000). PACAP and glutamate are co-stored in the retinohypothalamic tract. J. Comp. Neurol. 418, 147–155. [PubMed: 10701440]

Hatfield E, cacioppo JT, and Rapson RL (1994). Emotional Contagion (Cambridge University Press).

Hatori M, Le H, Vollmers C, Keding SR, Tanaka N, Buch T, Waisman A, Schmedt C, Jegla T, and Panda S (2008). Inducible ablation of melanopsin-expressing retinal ganglion cells reveals their central role in non-image forming visual responses. PLoS One 3, e2451. [PubMed: 18545654]

Hazan L, Zugaro M, and Buzsáki G (2006). Klusters, NeuroScope, NDManager: a free software suite for neurophysiological data processing and visualization. J. Neurosci. Methods 155, 207–216. [PubMed: 16580733]

Hirooka A, Hamada M, Fujiyama D, Takanami K, Kobayashi Y, Oti T, Katayama Y, Sakamoto T, and Sakamoto H (2021). The gastrin-releasing peptide/bombesin system revisited by a reverse-evolutionary study considering Xenopus. Sci. Rep. 11, 13315. [PubMed: 34172791]

Huberman AD, and Niell CM (2011). What can mice tell us about how vision works? Trends Neurosci. 34, 464–473. [PubMed: 21840069]

Ingle D (1968). Visual releasers of prey-catching behavior in frogs and toads. Brain Behav. Evol. 1, 500–518.

Ingle DJ (1981). New methods for analysis of vision in the gerbil. Behav. Brain Res. 3, 151–173. [PubMed: 7271985]

Ito S, and Feldheim DA (2018). The mouse superior colliculus: an emerging model for studying circuit formation and function. Front. Neural Circuits 12, 10. [PubMed: 29487505]

Itti L, and Koch C (2001). Computational modelling of visual attention. Nat. Rev. Neurosci. 2, 194–203. [PubMed: 11256080]

Jones JR, Chaturvedi S, Granados-Fuentes D, and Herzog ED (2021). Circadian neurons in the paraventricular nucleus entrain and sustain daily rhythms in glucocorticoids. Nat. Commun. 12, 5763. [PubMed: 34599158]

Kadir SN, Goodman DFM, and Harris KD (2014). High-dimensional cluster analysis with the masked EM algorithm. Neural Comput. 26, 2379–2394. [PubMed: 25149694]

Kalsbeek A, van Heerikhuize JJ, Wortel J, and Buijs RM (1996). A diurnal rhythm of stimulatory input to the hypothalamo-pituitary-adrenal system as revealed by timed intrahypothalamic administration of the vasopressin V1 antagonist. J. Neurosci. 16, 5555–5565. [PubMed: 8757267]

Kaneda K, Yanagawa Y, and Isa T (2012). Transient enhancement of inhibition following visual cortical lesions in the mouse superior colliculus. Eur. J. Neurosci. 36, 3066–3076. [PubMed: 22775357]

Karatsoreos IN, Yan L, LeSauter J, and Silver R (2004). Phenotype matters: identification of light-responsive cells in the mouse suprachiasmatic nucleus. J. Neurosci. 24, 68–75. [PubMed: 14715939]

Kim A, Keum S, and Shin HS (2019). Observational fear behavior in rodents as a model for empathy. Genes Brain Behav. 18, e12521. [PubMed: 30264490]

Kirouac GJ (2015). Placing the paraventricular nucleus of the thalamus within the brain circuits that control behavior. Neurosci. Biobehav. Rev. 56, 315–329. [PubMed: 26255593]

Kirouac GJ (2021). The paraventricular nucleus of the thalamus as an integrating and relay node in the brain anxiety network. Front. Behav. Neurosci. 15, 627633. [PubMed: 33732118]

Koch CE, Leinweber B, Drengberg BC, Blaum C, and Oster H (2017). Interaction between circadian rhythms and stress. Neurobiol. Stress 6, 57–67. [PubMed: 28229109]

Kolb H, Zhang L, and Dekorver L (1993). Differential staining of neurons in the human retina with antibodies to protein kinase C isozymes. Vis. Neurosci. 10, 341–351. [PubMed: 8485096]

Kuffler SW, and Eyzaguirre C (1955). Synaptic inhibition in an isolated nerve cell. J. Gen. Physiol. 39, 155–184. [PubMed: 13252239]

Kumar P, Wu H, McBride JL, Jung KE, Kim MH, Davidson BL, Lee SK, Shankar P, and Manjunath N (2007). Transvascular delivery of small interfering RNA to the central nervous system. Nature 448, 39–43. [PubMed: 17572664]

Kvitsiani D, Ranade S, Hangya B, Taniguchi H, Huang JZ, and Kepecs A (2013). Distinct behavioural and network correlates of two interneuron types in prefrontal cortex. Nature 498, 363–366. [PubMed: 23708967]

Lakin JL, Jefferis VE, Cheng CM, and Chartrand TL (2003). The chameleon effect as social glue: evidence for the evolutionary significance of nonconscious mimicry. J. Nonverbal Behav. 27, 145–162.

Lalic T, Steponenaite A, Wei L, Vasudevan SR, Mathie A, Peirson SN, Lall GS, and Cader MZ (2020). TRESK is a key regulator of nocturnal suprachiasmatic nucleus dynamics and light adaptive responses. Nat. Commun. 11, 4614. [PubMed: 32929069]

Langford DJ, Crager SE, Shehzad Z, Smith SB, Sotocinal SG, Levenstadt JS, Chanda ML, Levitin DJ, and Mogil JS (2006). Social modulation of pain as evidence for empathy in mice. Science 312, 1967–1970. [PubMed: 16809545]

Leopold DA (2012). Primary visual cortex: awareness and blindsight. Annu. Rev. Neurosci. 35, 91–109. [PubMed: 22715879]

Lettvin J, Maturana H, McCulloch W, and Pitts W (1959). What the frogs eye tells the frogs brain. Proc. IRE 47, 1940–1951.

Lucas RJ, Allen AE, Milosavljevic N, Storchi R, and Woelders T (2020). Can we see with melanopsin? Annu. Rev. Vis. Sci. 6, 453–468. [PubMed: 32491960]

Lucas RJ, Hattar S, Takao M, Berson DM, Foster RG, and Yau KW (2003). Diminished pupillary light reflex at high irradiances in melanopsin-knockout mice. Science 299, 245–247. [PubMed: 12522249]

Ma J, Zhao Z, Cui S, Liu F-Y, Yi M, and Wan Y (2019). A novel 3D-printed multi-drive system for synchronous electrophysiological recording in multiple brain regions. Front. Neurosci. 13, 1322. [PubMed: 31920492]

Madisen L, Mao T, Koch H, Zhuo JM, Berenyi A, Fujisawa S, Hsu YWA, Garcia AJ 3rd, Gu X, Zanella S, et al. (2012). A toolbox of Cre-dependent optogenetic transgenic mice for light-induced activation and silencing. Nat. Neurosci. 15, 793–802. [PubMed: 22446880]

Marques T, Summers MT, Fioreze G, Fridman M, Dias RF, Feller MB, and Petreanu L (2018). A role for mouse primary visual cortex in motion perception. Curr. Biol. 28, 1703–1713.e6. [PubMed: 29779878]

Mazuski C, Abel JH, Chen SP, Hermanstyne TO, Jones JR, Simon T, Doyle FJ 3rd, and Herzog ED (2018). Entrainment of circadian rhythms depends on firing rates and neuropeptide release of VIP SCN neurons. Neuron 99, 555–563.e5. [PubMed: 30017392]

Mazziotti R, Baroncelli L, Ceglia N, Chelini G, Sala GD, Magnan C, Napoli D, Putignano E, Silingardi D, Tola J, et al. (2017). Mir-132/212 is required for maturation of binocular matching of orientation preference and depth perception. Nat. Commun. 8, 15488. [PubMed: 28534484]

Menaker M, Moreira LF, and Tosini G (1997). Evolution of circadian organization in vertebrates. Braz. J. Med. Biol. Res. 30, 305–313. [PubMed: 9246228]

Michel S, Itri J, Han JH, Gniotczynski K, and Colwell CS (2006). Regulation of glutamatergic signalling by PACAP in the mammalian suprachiasmatic nucleus. BMC Neurosci. 7, 15. [PubMed: 16483357]

Miller CT, Gire D, Hoke K, Huk AC, Kelley D, Leopold DA, Smear MC, Theunissen F, Yartsev M, and Niell CM (2022). Natural behavior is the language of the brain. Curr. Biol. 32, R482–R493. [PubMed: 35609550]

Misery L, Dutray S, Chastaing M, Schollhammer M, Consoli SG, and Consoli SM (2018). Psychogenic itch. Transl. Psychiatry 8, 52. [PubMed: 29491364]

Mogil JS (2019). Mice are People too: increasing evidence for cognitive, emotional and social capabilities in Laboratory rodents. Can. Psychol./Psychol. Canad. 60, 14–20.

Moore RY, Speh JC, and Leak RK (2002). Suprachiasmatic nucleus organization. Cell Tissue Res. 309, 89–98. [PubMed: 12111539]

Morin LP, and Allen CN (2006). The circadian visual system, 2005. Brain Res. Rev. 51, 1–60. [PubMed: 16337005]

Mouland JW, Stinchcombe AR, Forger DB, Brown TM, and Lucas RJ (2017). Responses to spatial contrast in the mouse suprachiasmatic nuclei. Curr. Biol. 27, 1633–1640.e3. [PubMed: 28528901]

Munanairi A, Liu XY, Barry DM, Yang Q, Yin JB, Jin H, Li H, Meng QT, Peng JH, Wu ZY, et al. (2018). Non-canonical Opioid signaling inhibits itch transmission in the spinal cord of mice. Cell Rep. 23, 866–877. [PubMed: 29669290]

Niell CM, and Stryker MP (2010). Modulation of visual responses by behavioral state in mouse visual cortex. Neuron 65, 472–479. [PubMed: 20188652]

Overstreet DH, Keeney A, and Hogg S (2004). Antidepressant effects of citalopram and CRF receptor antagonist CP-154, 526 in a rat model of depression. Eur. J. Pharmacol. 492, 195–201. [PubMed: 15178365]

Penzo MA, and Gao C (2021). The paraventricular nucleus of the thalamus: an integrative node underlying homeostatic behavior. Trends Neurosci. 44, 538–549. [PubMed: 33775435]

Perkel DH, and Mulloney B (1974). Motor pattern production in reciprocally inhibitory neurons exhibiting postinhibitory rebound. Science 185, 181–183. [PubMed: 4834220]

Perkel DH, Schulman JH, Bullock TH, Moore GP, and Segundo JP (1964). Pacemaker neurons: effects of regularly spaced synaptic input. Science 145, 61–63. [PubMed: 14162696]

Prete FR (2004). Complex Worlds from Simpler Nervous Systems (The MIT Press).

Prochazkova E, and Kret ME (2017). Connecting minds and sharing emotions through mimicry: a neurocognitive model of emotional contagion. Neurosci. Biobehav. Rev. 80, 99–114. [PubMed: 28506927]

Provencio I, Jiang G, De Grip WJ, Hayes WP, and Rollag MD (1998). Melanopsin: an opsin in melanophores, brain, and eye. Proc. Natl. Acad. Sci. USA 95, 340–345. [PubMed: 9419377]

Provine RR (2012). Curious Behavior (The Belknap Press of Harvard University Press).

Prusky GT, and Douglas RM (2004). Characterization of mouse cortical spatial vision. Vision Res. 44, 3411–3418. [PubMed: 15536009]

Rakic P (2009). Evolution of the neocortex: a perspective from developmental biology. Nat. Rev. Neurosci. 10, 724–735. [PubMed: 19763105]

Ross RA, Leon S, Madara JC, Schafer D, Fergani C, Maguire CA, Verstegen AM, Brengle E, Kong D, Herbison AE, et al. (2018). PACAP neurons in the ventral premammillary nucleus regulate reproductive function in the female mouse. Elife 7, e35960. [PubMed: 29905528]

Ruby NF, Brennan TJ, Xie X, Cao V, Franken P, Heller HC, and O'Hara BF (2002). Role of melanopsin in circadian responses to light. Science 298, 2211–2213. [PubMed: 12481140]

Ruether K, Feigenspan A, Pirngruber J, Leitges M, Baehr W, and Strauss O (2010). PKC{alpha} is essential for the proper activation and termination of rod bipolar cell response. Invest. Ophthalmol. Vis. Sci. 51, 6051–6058. [PubMed: 20554612]

Schaap J, and Meijer JH (2001). Opposing effects of behavioural activity and light on neurons of the suprachiasmatic nucleus. Eur. J. Neurosci. 13, 1955–1962. [PubMed: 11403689]

Schindelin J, Arganda-Carreras I, Frise E, Kaynig V, Longair M, Pietzsch T, Preibisch S, Rueden C, Saalfeld S, Schmid B, et al. (2012). Fiji: an open-source platform for biological-image analysis. Nat. Methods 9, 676–682. [PubMed: 22743772]

Schmidt TM, Do MTH, Dacey D, Lucas R, Hattar S, and Matynia A (2011). Melanopsin-positive intrinsically photosensitive retinal ganglion cells: from form to function. J. Neurosci. 31, 16094–16101. [PubMed: 22072661]

Schneider GE (1969). Two visual systems. Science 163, 895–902. [PubMed: 5763873]

Schut C, Grossman S, Gieler U, Kupfer J, and Yosipovitch G (2015). Contagious itch: what we know and what we would like to know. Front. Hum. Neurosci. 9, 57. [PubMed: 25717300]

Shanks JA, Ito S, Schaevitz L, Yamada J, Chen B, Litke A, and Feldheim DA (2016). Corticothalamic axons are essential for retinal ganglion cell axon targeting to the mouse dorsal lateral geniculate nucleus. J. Neurosci. 36, 5252–5263. [PubMed: 27170123]

Stinchcombe AR, Mouland JW, Wong KY, Lucas RJ, and Forger DB (2017). Multiplexing visual signals in the suprachiasmatic nuclei. Cell Rep. 21, 1418–1425. [PubMed: 29117548]

Sun YG, and Chen ZF (2007). A gastrin-releasing peptide receptor mediates the itch sensation in the spinal cord. Nature 448, 700–703. [PubMed: 17653196]

Sun YG, Zhao ZQ, Meng XL, Yin J, Liu XY, and Chen ZF (2009). Cellular basis of itch sensation. Science 325, 1531–1534. [PubMed: 19661382]

Takanami K, Oti T, Kobayashi Y, Hasegawa K, Ito T, Tsutsui N, Ueda Y, Carstens E, Sakamoto T, and Sakamoto H (2022). Characterization of the expression of gastrin-releasing peptide and its receptor in the trigeminal and spinal somatosensory systems of Japanese macaque monkeys: insight into humans. J. Comp. Neurol. 530, 2804–2819. [PubMed: 35686563]

Takao K, and Miyakawa T (2006). Light/dark transition test for mice. J. Vis. Exp. 104.

Tan CL, Cooke EK, Leib DE, Lin YC, Daly GE, Zimmerman CA, and Knight ZA (2016). Warm-sensitive neurons that control body temperature. Cell 167, 47–59.e15. [PubMed: 27616062]

Tian J, and Uchida N (2015). Habenula lesions reveal that multiple mechanisms underlie dopamine prediction errors. Neuron 87, 1304–1316. [PubMed: 26365765]

Tran NM, Shekhar K, Whitney IE, Jacobi A, Benhar I, Hong G, Yan W, Adiconis X, Arnold ME, Lee JM, et al. (2019). Single-cell profiles of retinal ganglion cells differing in resilience to injury reveal neuroprotective genes. Neuron 104, 1039–1055.e12. [PubMed: 31784286]

Ulrich-Lai YM, and Herman JP (2009). Neural regulation of endocrine and autonomic stress responses. Nat. Rev. Neurosci. 10, 397–409. [PubMed: 19469025]

Van der Werf YD, Witter MP, and Groenewegen HJ (2002). The intralaminar and midline nuclei of the thalamus. Anatomical and functional evidence for participation in processes of arousal and awareness. Brain Res. Brain Res. Rev. 39, 107–140. [PubMed: 12423763]

Wang L, McAlonan K, Goldstein S, Gerfen CR, and Krauzlis RJ (2020). A causal role for mouse superior colliculus in visual perceptual decision-making. J. Neurosci. 40, 3768–3782. [PubMed: 32253361]

Wei P, Liu N, Zhang Z, Liu X, Tang Y, He X, Wu B, Zhou Z, Liu Y, Li J, et al. (2015). Processing of visually evoked innate fear by a non-canonical thalamic pathway. Nat. Commun. 6, 8228. [PubMed: 26293832]

Weiskrantz L (2009). Blindsight: A Case Study Spanning 35 Years and New Developments, The Second Edition edn (Oxford University Press).

Welsh DK, Logothetis DE, Meister M, and Reppert SM (1995). Individual neurons dissociated from rat suprachiasmatic nucleus express independently phased circadian firing rhythms. Neuron 14, 697–706. [PubMed: 7718233]

Winans SS (1967). Visual form discrimination after removal of the visual cortex in cats. Science 158, 944–946. [PubMed: 6054170]

Yu YQ, Barry DM, Hao Y, Liu XT, and Chen ZF (2017). Molecular and neural basis of contagious itch behavior in mice. Science 355, 1072–1076. [PubMed: 28280205]

Zariwala HA, Borghuis BG, Hoogland TM, Madisen L, Tian L, De Zeeuw CI, Zeng H, Looger LL, Svoboda K, and Chen TW (2012). A Cre-dependent GCaMP3 reporter mouse for neuronal imaging in vivo. J. Neurosci. 32, 3131–3141. [PubMed: 22378886]

Zentall TR (2006). Imitation: definitions, evidence, and mechanisms. Anim. Cogn. 9, 335–353. [PubMed: 17024510]

Highlights

- SCN-projecting ipRGCs are necessary and sufficient for contagious itch behavior
- Melanopsin is not required for contagious itch behavior
- PACAP transmits itch information to SCN GRP neurons via PAC1R
- SCN GRPR neurons display itch-specific neural dynamics and firing patterns

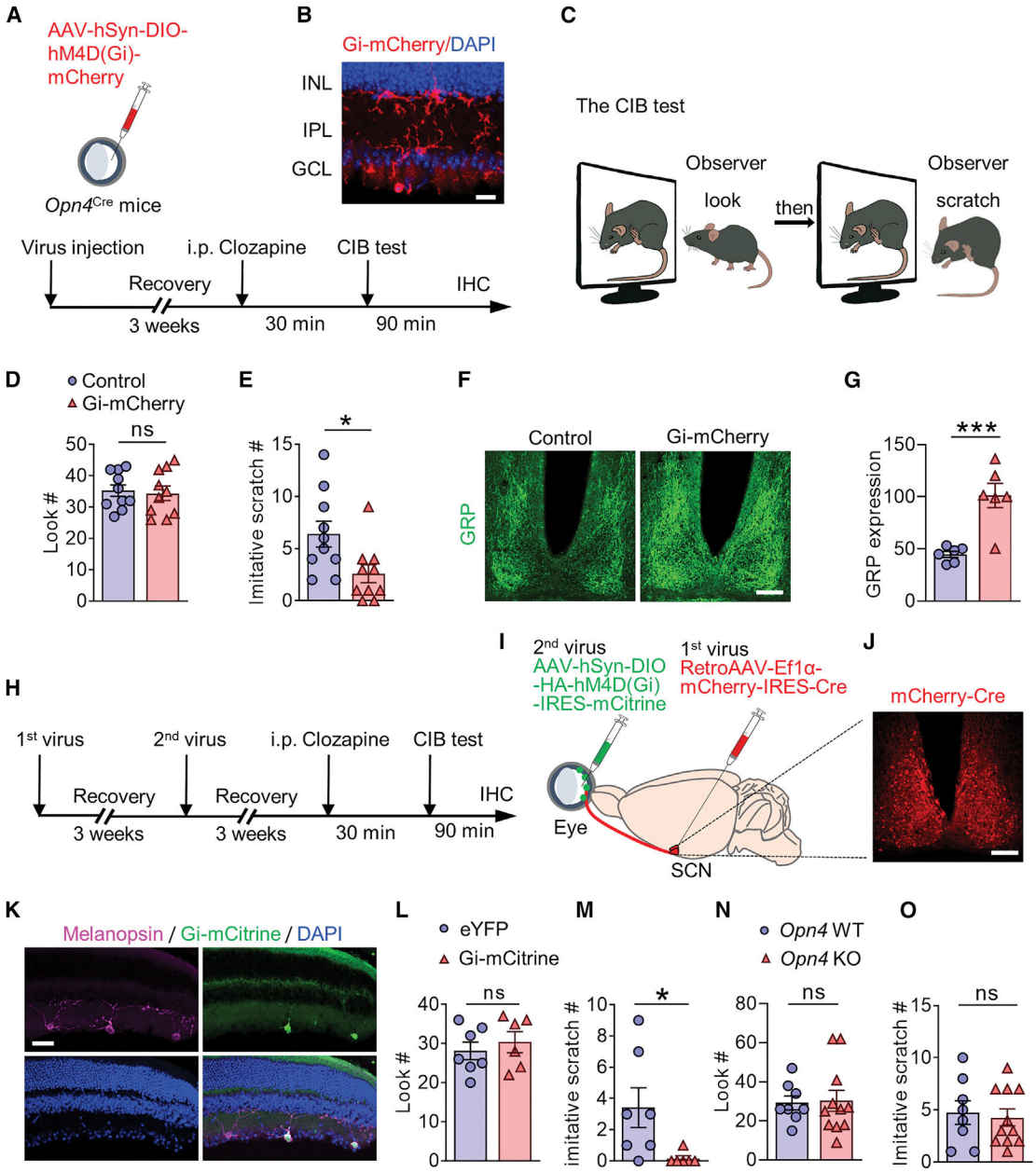

Figure 1. ipRGCs are required for CIB

(A) Schedule and schematic illustrating chemogenetic inhibition of ipRGCs by intravitreal injection of AAV-hSyn-DIO-h4MD(Gi)-mCherry in *Opn4*^{Cre} mice.

(B) IHC image showing Gi-mCherry expression in the retina of *Opn4*^{Cre} mice. Scale bar, 20 μm. n = 3.

(C) Cartoon illustrating the CIB paradigm.

(D and E) Mean number of look (D) (t = 0.3064, df = 18, p = 0.7628) and imitative scratches (E) (t = 2.519, df = 18, p = 0.0214) of mCherry control and Gi-mCherry mice. n = 10/group.

(F) GRP expression in the SCN of *Opn4*^{Cre} mice in mCherry control group and Gi-mCherry group after the CIB test. Scale bar, 100 μm.

(G) Quantification of GRP expression in (F), t = 4.639, df = 10, p = 0.0009, n = 6/group.

(H) Schedule of chemogenetic inhibition of SCN projecting-ipRGCs for the CIB test.
(I) Schematic illustration of two-step virus injection in H: 1st virus RetroAAV-Ef1a-mCherry-IRES-Cre was injected in the SCN of C57BL/6J mice. Three weeks later, the 2nd virus AAV-hSyn-DIO-HA-hM4D(Gi)-IRES-mCitrine was intravitreally injected.
(J) mCherry-Cre (red) expression in the SCN after virus injection. Scale bar, 100 μm.
(K) IHC image showing melanpsin (magenta), Gi-mCitrine (green), DAPI (blue) in the retina. Scale bar, 100 μm.
(L and M) Mean number of look (L) ($t = 0.6355$, $df = 11$, $p = 0.5381$), mean number of imitative scratches (M) ($t = 2.349$, $df = 11$, $p = 0.0386$) of mice with eYFP control (n = 7) or Gi-mCitrine (n = 6).
(N and O) Mean number of look (N) ($t = 0.1599$, $df = 17$, $p = 0.8748$); mean number of imitative scratch (O) ($t = 0.3509$, $df = 17$, $p = 0.7300$) of *Opn4* KO (n = 11) and WT littermates (n = 8).
Data are presented as mean ± SEM. Unpaired t test in (D, E, G, and L–O). ns, not significant. *$p < 0.05$, **$p < 0.01$, ***$p < 0.001$.

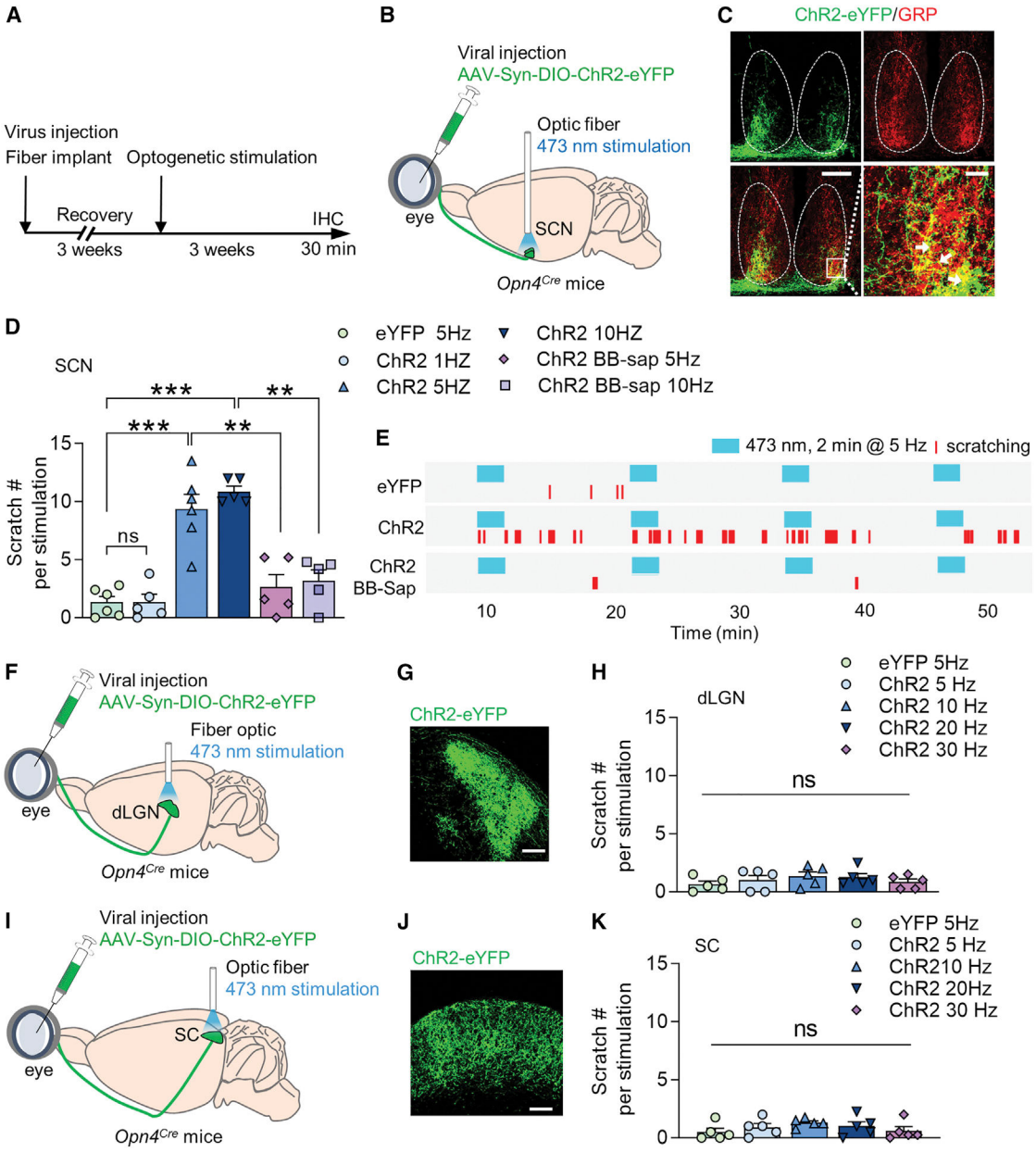

Figure 2. Optic activation of ipRGCs terminal in the SCN, but not dLGN or SC, evoked scratching behavior

(A and B) Schedule and schematic illustration of intravitreal injection of AAV-Syn-DIO-ChR2-eYFP and unilateral optic fiber implantation into the SCN of *Opn4*^{Cre} mice.

(C) Overlapping expression of ChR2 eYFP (green) and GRP (red) in the SCN of *Opn4*^{Cre} mice. The terminal of ipRGCs labled by ChR2-eYFP broadly innervate the ventral side of the SCN. Scale bars, 100 μm (bottom left) and 20 μm (bottom right). n = 3.

(D) Mean number of scratches induced by photostimulation (473 nm for 2 min at 1, 5, or 10 Hz) in eYFP control, ChR2 and ChR2 BB-Sap mice. n = 5~6 for each group ($F(6, 30) = 2.906$, $p < 0.0001$).

(E) Representative raster plots of scratching behaviors induced by photo-stimulation (473 nm for 2 min at 5 Hz) of eYFP control, ChR2 and ChR2 BB-sap mice.
(F) Schematic illustration of intravitreal injection of AAV-Syn-DIO-ChR2-eYFP and unilateral fiber-optic implantation into dLGN of *Opn4*^{Cre} mice.
(G) dLGN projecting terminals of ipRGCs labeled by ChR2-eYFP after intravitreal injection.
(H) Mean number of scratches induced by photostimulation (473 nm for 2 min at 5, 10, 20, or 30 Hz) in eYFP control and ChR2 mice ($F(4, 20) = 0.2870$, $p = 0.7387$). n = 5 for each group.
(I) Schematic illustration of intravitreal injection of AAV-Syn-DIO-ChR2-eYFP and unilateral optic fiber implantation into the SC of *Opn4*^{Cre} mice.
(J) SC-projecting ipRGC terminals labeled by ChR2-eYFP after intravitreal injection.
(K) Mean number of scratches induced by photostimulation (473 nm for 2 min at 5, 10, 20, or 30 Hz) in eYFP control and ChR2 mice ($F(4, 20) = 0.2743$, $p = 0.9976$). n = 5 for each group.
One-way ANOVA with Tukey's multiple comparisons test (D, H, and K). *$p < 0.05$, **$p < 0.01$, ***$p < 0.001$; ns, not significant.

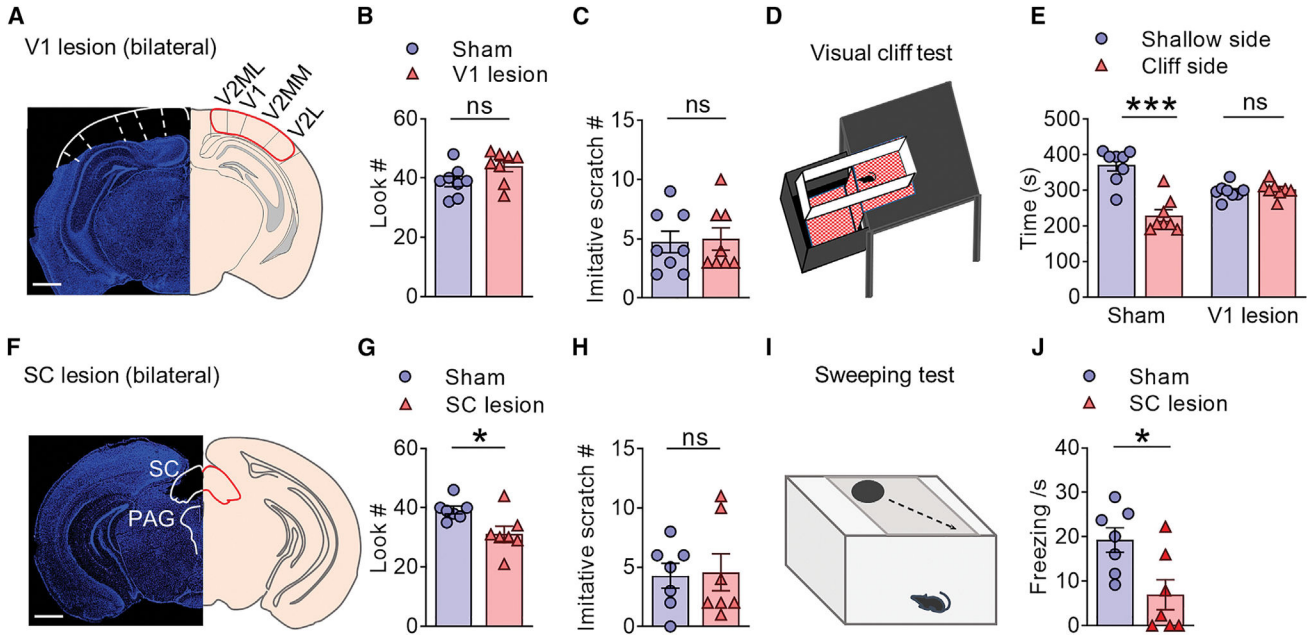

Figure 3. Visual cortex and superior colliculus are not required for contagious itch

(A) Coronal section of the brain stained with DAPI (blue) showing visual cortex lesion (left) and corresponding anatomical location (right). Scale bar, 500 μm.

(B and C) Mean number of look (B) ($t = 1.986$, $df = 14$, $p = 0.0670$) and imitative scratch behaviors (C) ($t = 0.1895$, $df = 14$, $p = 0.8524$) of mice with visual sham surgery and visual cortex lesion.

(D) Cartoon illustrating the visual cliff test.

(E) Left: mice with sham surgery spent significantly shorter time on the cliff side than the shallow side, indicating a normal depth perception. Right: mice with visual cortex lesion spent a comparable amount of time on either side, indicating a loss of depth perception. $F(1, 14) = 31.94$, $p < 0.0001$.

(F) Coronal section of the brain (blue, DAPI) showing SC lesion (left) and corresponding anatomical location. SC, superior colliculus. PAG, periaqueductal gray. Scale bar, 500 μm.

(G and H) Mean number of look (G) ($t = 2.752$, $df = 12$, $p = 0.0175$) and imitative scratch behaviors (H) ($t = 0.1516$, $df = 12$, $p = 0.8820$) of mice with SC lesion.

(I) Cartoon illustrating the sweeping test.

(J) SC lesion significantly reduces freezing behavior during sweeping test relative to the control ($t = 2.818$, $df = 12$, $p = 0.0155$). n = 8 mice/group for V1 lesion, n = 7 mice/group for SC lesion.

Data are presented as mean ± SEM. Unpaired t test in (B, C, G, H, and J). Two-way ANOVA in (E). ns, not significant. *$p < 0.05$, ***$p < 0.001$.

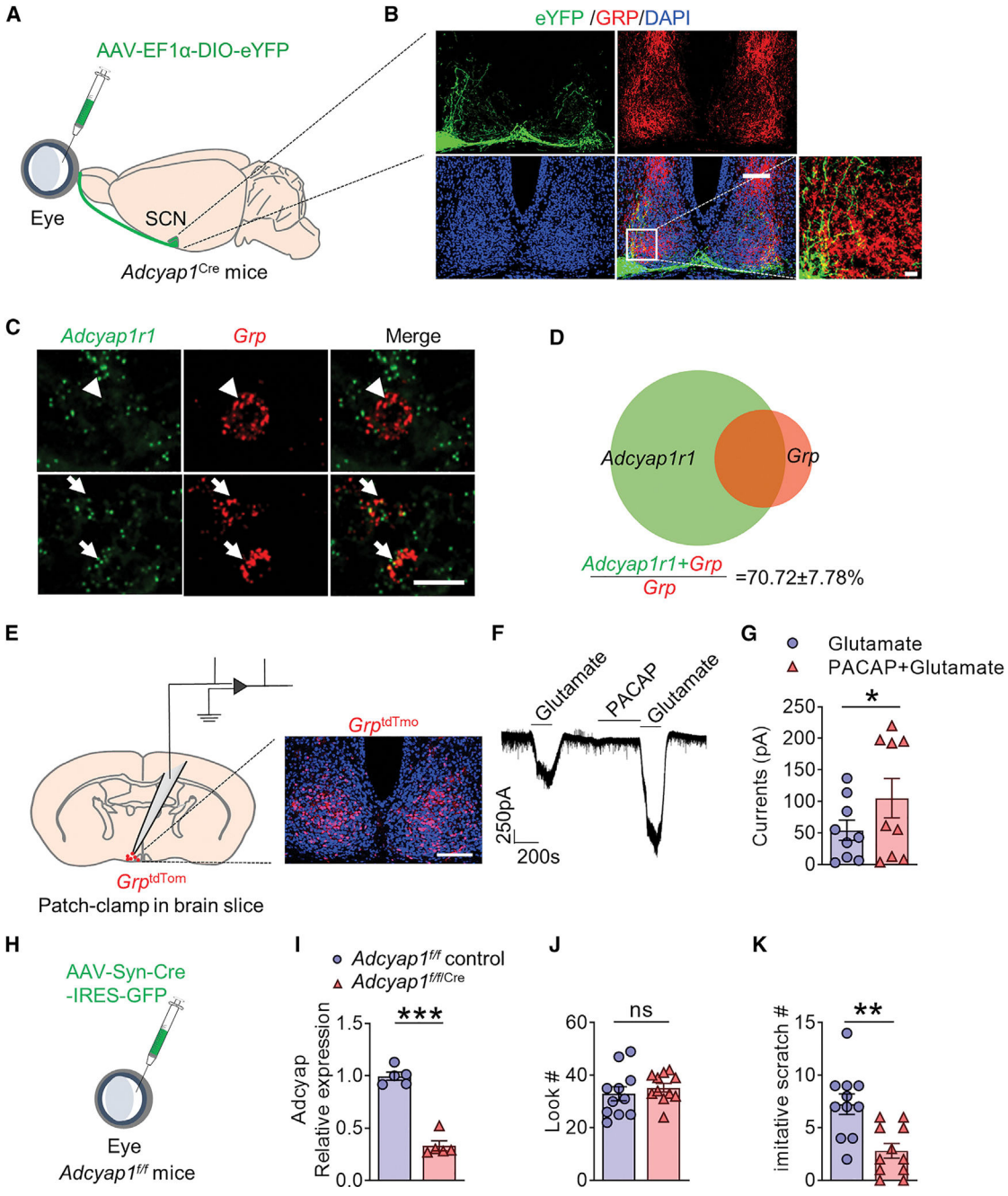

Figure 4. ipRGCs activate GRP neurons through PACAP

(A) Schematic of intravitreal injection of AAV-EF1α-DIO-eYFP virus in *Adcyap1*^{Cre} mice.

(B) Overlapping expression of eYFP (green) and GRP (red) in the SCN of *Adcyap1*^{Cre} mice. Scale bars, 100 μm (top) and 20 μm (bottom right). n = 3.

(C) Representative RNAscope image showing the overlapping and non-overlapping of *Adcyap1r1* and *Grp* in the SCN. Scale bar, 10 μm.

(D) Venn diagram showing that 70.72% ± 7.78% of *Grp* cells express *Adcyap1r1*. n = 3.

(E) Schematic of brain slice recording of SCN *Grp*^{tdTom} neurons obtained from *Grp*$^{Cre/tdTom}$ mice (left); a representative image showing *Grp*^{tdTom} neurons in the SCN of *Grp*$^{Cre/tdTom}$ mice (right). Scale bar, 100 μm.

(F) A representative trace showing that PACAP (10 mM) enhanced glutamate-evoked current in *Grp*^{tdTom} neurons.

(G) The mean current induced by glutamate with or without PACAP pretreatment (9 of 16 *Grp* cells showed enhanced glutamate current, n = 4 mice). t = 2.809, df = 8, p = 0.0229.

(H) Schematic of intravitreal injection of AAV-hSyn-Cre-IRES-eGFP or the control eYFP virus in *Adcyap1*$^{f/f}$ mice (*Adcyap1*$^{f/f/Cre}$ or *Adcyap1*$^{f/f}$ control mice).

(I) Comparison of *Adcyap1* mRNA expression in the retina of *Adcyap1*$^{f/f/Cre}$ or control mice (t = 10.81, df = 8, p < 0.0001), n = 5.

(J and K) Mean number of look (J) (t = 0.7213, df = 20, p = 0.4791) and imitative scratch behaviors (K) (t = 3.719, df = 20, p = 0.0014) of *Adcyap1*$^{f/f/Cre}$ (n = 11) or *Adcyap1*$^{f/f}$ control (n = 11) mice.

Data are presented as mean ± SEM. Unpaired t test in (G and I–K). ns, not significant. *p < 0.05, **p < 0.01, ***p < 0.001.

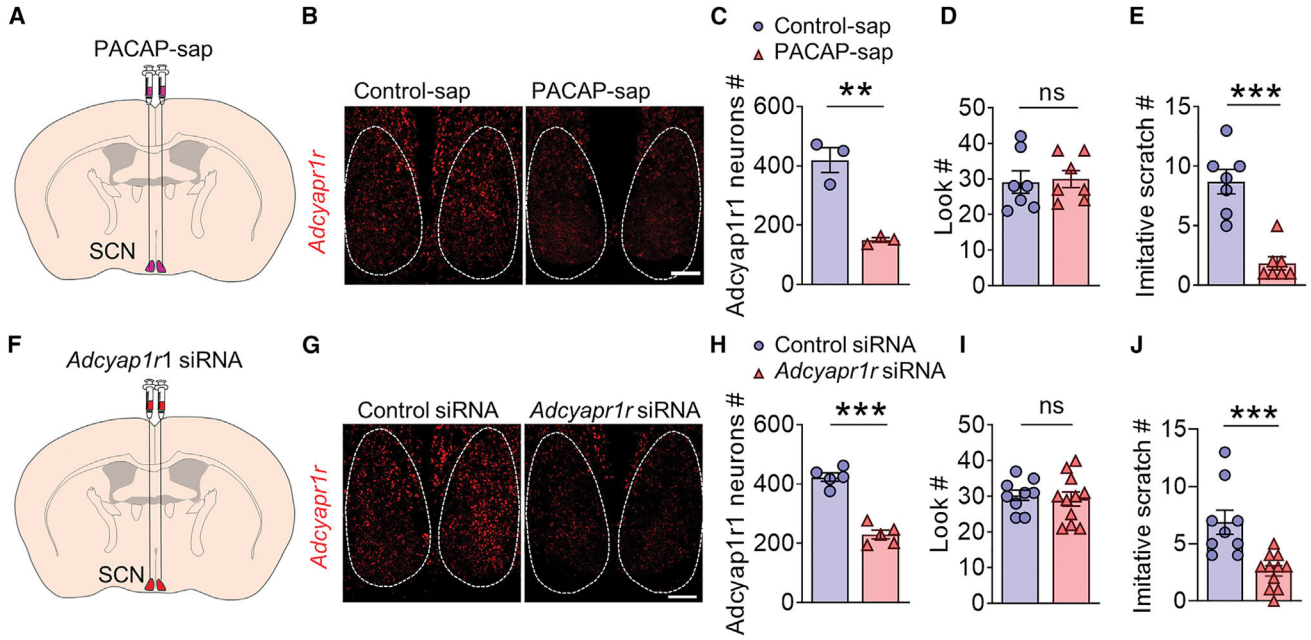

Figure 5. PACAP mediated CIB through the PAC1 receptor in SCN GRP neurons

(A) Schedule of ablation of PAC1 neurons by PACAP-saporin (PACAP-sap) injection into the SCN.

(B) RNAscope ISH images showing the expression of *Adcyap1r1* (red) in the SCN of mice with control-sap and PACAP-sap. Scale bar, 100 μm.

(C) Mean expression of *Adcyap1r1* mRNA ($t = 6.330$, $df = 4$, $p = 0.0032$) in the SCN after Control-sap and PACAP-sap treatment. $n = 3$.

(D and E) Mean number of look (D) ($t = 0.2181$, $df = 12$, $p = 0.4155$) and imitative scratch behaviors (E) ($t = 5.923$, $df = 12$, $p < 0.0001$) of mice with control-sap ($n = 7$) and PACAP-sap ($n = 7$).

(F) Schematic illustration of bilateral injection of *Adcyapr1r1* siRNA in SCN.

(G) Representative RNAscope image showing reduced expression of *Adcyapr1r1* in the SCN after *Adcyapr1r1* siRNA injection compared with the Control siRNA group. Scale bar, 100 μm.

(H) Mean expression of *Adcyap1r1* mRNA ($t = 9.342$, $df = 8$, $p < 0.001$) in the SCN after Control siRNA and *Adcyapr1r1* siRNA treatment. $n = 5$.

(I and J) Mean number of look (I) ($t = 0.4100$, $df = 18$, $p = 0.6866$) mean number of imitative scratch (J) ($t = 3.986$, $df = 18$, $p = 0.0009$) of Control siRNA ($n = 9$) or *Adcyapr1r1* siRNA ($n = 11$) treated mice.

Data are presented as mean ± SEM. Unpaired t test in (C–E and H–J). ns, not significant; *$p < 0.05$, **$p < 0.01$, ***$p < 0.001$.

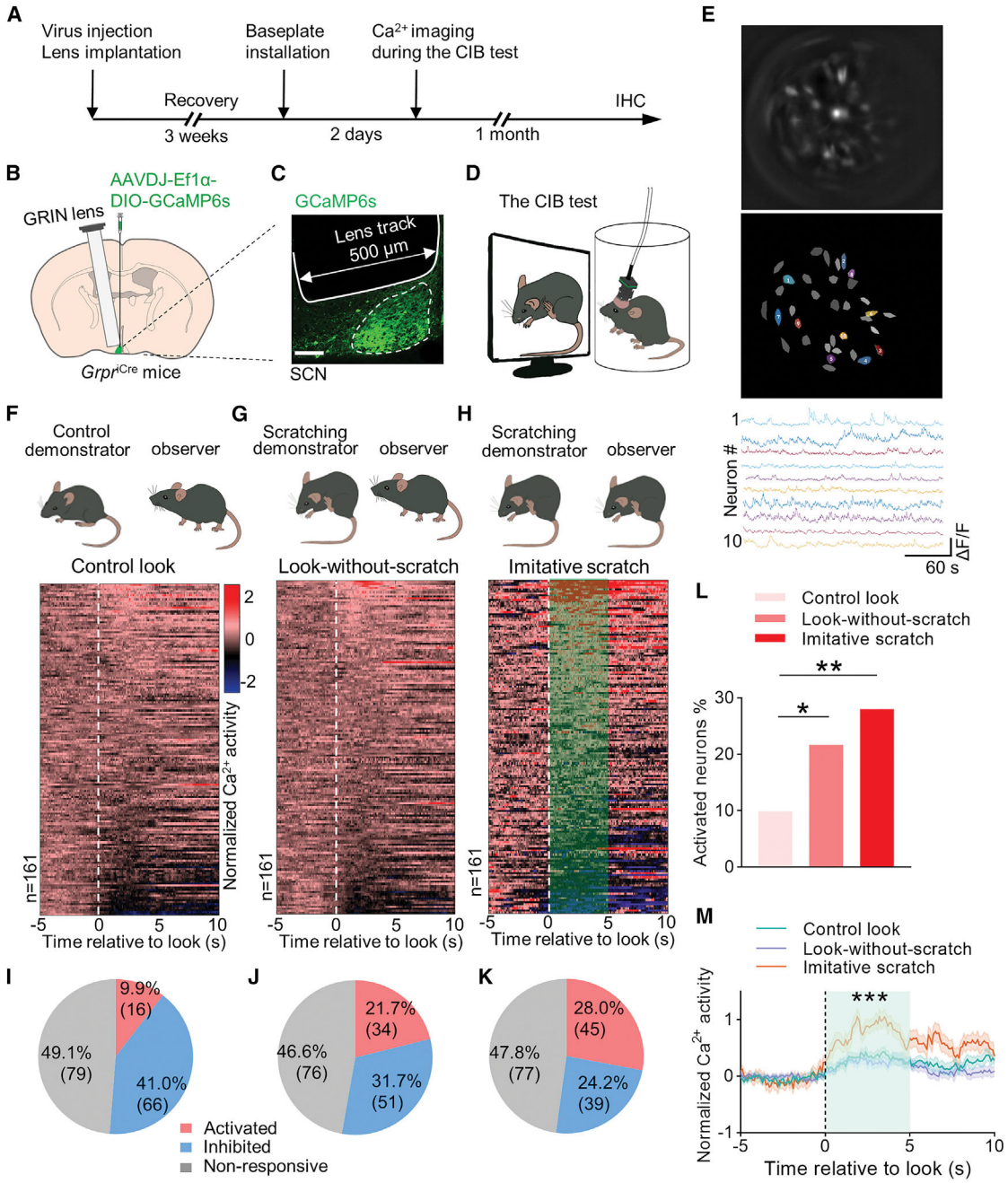

Figure 6. *In vivo* Ca^{2+} imaging of the responses of GRPR neurons to scratching motion

(A) Schedule of *in vivo* Ca^{2+} imaging during the CIB test.

(B) Unilateral injection of AAVDJ-EF1α-DIO-GCaMP6s and implantation of GRIN lens into the left SCN of *Grpr*^{iCre} mice. GRIN lens (500 μm diameter) was positioned above GCaMP6s-expressing SCN (~300 μm diameter; 6 mm depth).

(C) Representative image showing the GCaMP6s virus expression in SCN and the lens track.

(D) A *Grpr*^{iCre} mouse with a head-mounted miniscope in a cylinder watches a mouse scratching video.

(E) Schematized cell map of dynamic GRPR cells in the whole field view (upper two panels); independent component analysis derived GRPR neuron activity traces (bottom panel).

(F) Cartoon illustrating an observer mouse looking at an ambulating mouse demonstrator (control, upper panel). Heatmap of normalized Ca^{2+} activation patterns from all individual GRPR cells recorded corresponding to the control look behavior (without any other associated behavior) toward the control demonstrator (lower panel). 0 s time point indicates the onset of look.

(G) Cartoon illustrating an observer looking at a scratching demonstrator without ensuing scratching behavior (look-without-scratch, upper panel). Heatmap of normalized Ca^{2+} activation patterns from all individual GRPR neurons recorded corresponding to the look-without-scratch behavior toward a scratching demonstrator (lower panel).

(H) Cartoon illustrating an observer mouse displays an imitative scratch behavior (upper panel). Heatmap of normalized Ca^{2+} activity of individual GRPR cells corresponding to the look of imitative scratch in CIB during watching the scratching demonstrator. Imitative scratch behavior is defined as it occurring within 5 s following the look behavior.

(I–K) Classification of GRPR cells according to the response to the control look (I), the look-without-scratch (J), and imitative scratches (look-and-scratch) (K).

(L) Percentage of GRPR cells showing activated Ca^{2+} response corresponding to the control look, look-without-scratch and imitative scratch.

(M) Mean Ca^{2+} traces of neurons with activated Ca^{2+} response corresponding to control look (16 neurons), look-without-scratch (34 neurons), and imitative scratch (45 neurons) ($F = 20.81$, $p < 0.0001$).

A total of 161 neurons were recorded from 8 mice. Contingency chi-square test in (L). One-way ANOVA test in (M) for the area under the curve. *$p < 0.05$, **$p < 0.01$, ***$p < 0.001$.

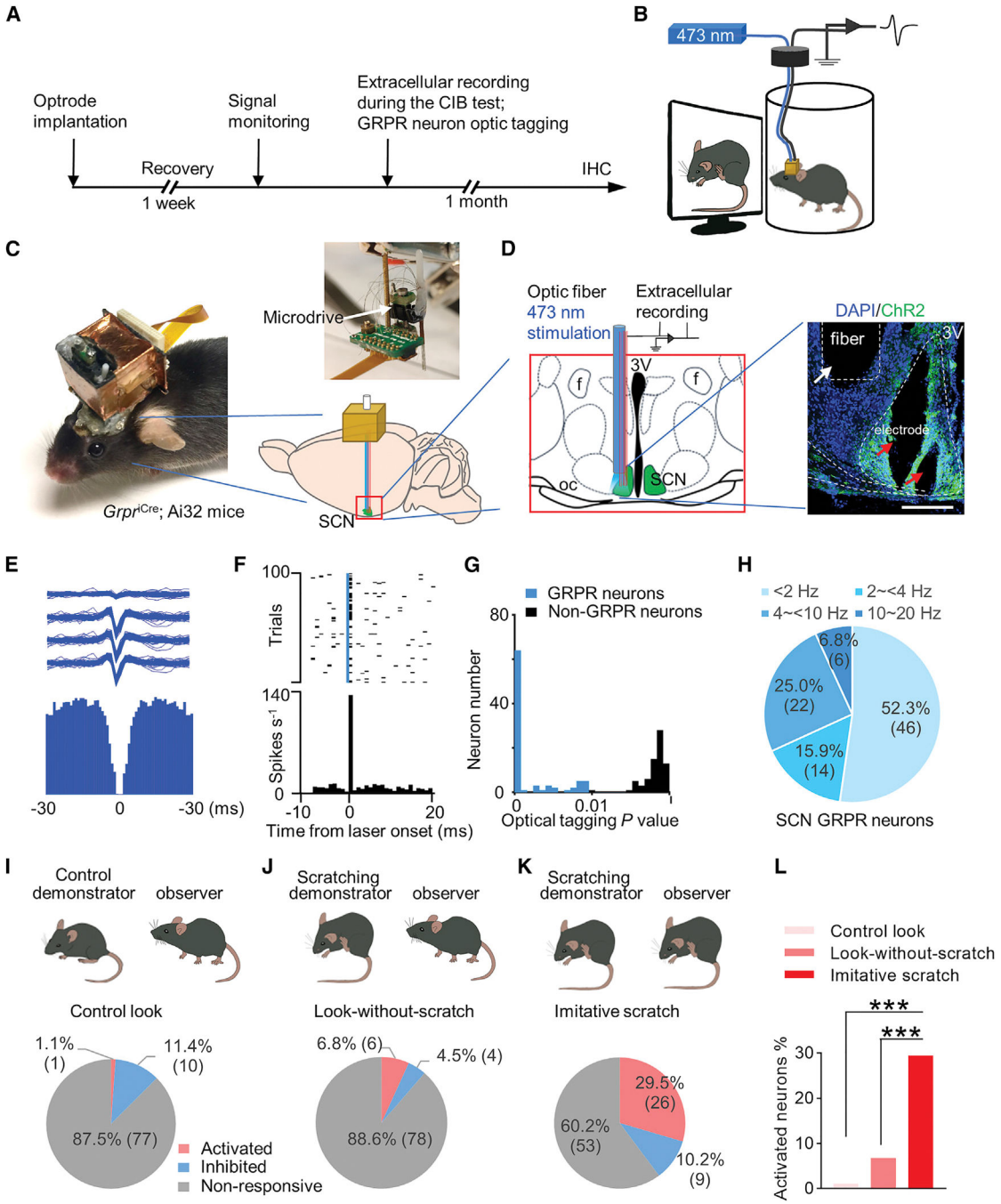

Figure 7. *In vivo* multichannel extracellular recording of the response of GRPR neurons to scratching motion

(A) Experimental procedure of *in vivo* multichannel extracellular recording of SCN GRPR neurons of *Grpr*^{iCre}; Ai32 mice during the CIB test.

(B) Cartoon showing the electrophysiological recording of SCN GRPR neurons. Note that the *Grpr*^{iCre}; Ai32 mouse with a self-made optrode with a 3D-printed protective hat, which was wrapped with copper tape and connected to the system ground to gain extra protection against electrical noise.

(C) Photos showing the head of the *Grpr*^{iCre}; Ai32 mouse with the hat and an optrode, consisting of eight tetrodes and optical fiber with a microdrive (top right) that enables the D-V directional movement of the optrode in the brain and a cartoon showing the optrode implanted into the SCN of the *Grpr*^{iCre}; *Ai32* mouse brain (bottom right).
(D) Left: schematic of optrode implantation in the left side of the SCN. The optical fiber was connected to a 473 nm blue laser for the identification of ChR2-tagging GRPR neurons. Right: a representative image showing the histology of optical fiber (white arrow) and electrodes (red arrows) in the left side of the SCN.
(E) Waveform (top) and auto-correlogram (bottom) of one well-isolated neuron from the SCN of *Grpr*^{iCre}; *Ai32* mouse. A total of well-isolated 159 SCN neurons were sorted out from 7 *Grpr*^{iCre}: *Ai32* mice.
(F) Optogenetic identification of GRPR neurons. Spike raster (top) and peri-stimulus time histogram (PSTH) (bottom) for an identified GRPR neuron aligned to the onset of blue light pulse (top, blue line, 473 nm, duration, 1 ms; power, 1 to 4 mW; frequency, 20 Hz).
(G) Histogram of stimulus-associated spike latency test (SALT) for optical tagging showing p value distribution ($p < 0.01$, blue). A total of 88 neurons were identified as GRPR neurons.
(H) Distribution of 88 GRPR neurons according to their baseline firing rates.
(I–K) Classification of 88 GRPR neurons based on their excitatory, inhibitory and no responses under three behavioral conditions: the control look (I), look-without-scratch (J), and imitative scratch (K).
(L) Comparison of the percentage of GRPR neurons that were activated under three behavioral conditions.
Chi-square test in (L), ***$p < 0.001$.

REAGENT or RESOURCE	SOURCE	IDENTIFIER
Antibodies		
Rabbit anti-melanopsin	Advanced Targeting Systems	Cat # IT-44-25; RRID: AB_1266797
Rabbit anti-GRP	Immunostar	Cat #20073; RRID: AB_572221
Chicken anti-GFP	Aves Labs	Cat #GFP-1020; RRID: AB_10000240
Mouse anti-mCherry	Developmental Studies Hybridoma Bank	Cat #3A11; RRID: AB_2617430
Guinea Pig anti-RBPMS	PhosphoSolutions	Cat #1832-RBPMS; RRID: AB_2492226
Rabbit anti-PKCα	Santa Cruz	Cat #sc-208; RRID: AB_2168668
Rabbit anti-PKCβ	Santa Cruz	Cat #sc-209; RRID: AB_2168968
Rabbit anti-GRPR	MBL International	Cat #MC-831; RRID: AB_591750
Rabbit anti-AVP	Immunostar	Cat #20069; RRID: AB_572219
Rabbit anti-VIP	Immunostar	Cat #20077; RRID: AB_572270
Cy3-conjugated Donkey anti-mouse	Jackson Immuno-Research	Cat #715-165-150; RRID: AB_2340813
Cy3-conjugated Donkey anti-rabbit	Jackson Immuno-Research	Cat #711-165-152; RRID: AB_2307443
Alexa Fluor® AffiniPure donkey anti-chicken	Jackson Immuno-Research	Cat #703-095-155; RRID:AB_2340356
RVG-9R	Bachem AG	Cat #H-7502.0500
Bacterial and virus strains		
AAV5-EF1 α-DIO-ChR2-(H134R)-eYFP	Hope Center Viral Vectors Core	N/A
AAV8-hSyn-DIO-h4MDi-mCherry	Hope Center Viral Vectors Core	N/A
AAV5-EF1 α-DIO-eYFP	Hope Center Viral Vectors Core	N/A
AAVDJ-EF1 α-DIO-GCaMP6s	Stanford Viral Vector Core	RRID: GVVC-AAV-165
RetroAAV-Ef1a-mCherry-IRES-Cre	Fenno et al. (2014)	RRID: Addgene_ 55632-AAVrg
AAV5-hSyn-DIO-HA-hM4D(Gi)-IRES-mCitrine	Bryan Roth	RRID: Addgene_50455-AAV5
AAV2-Syn-Cre-IRES-GFP	Hope Center Viral Vectors Core	N/A
RetroAAV-Ef1 α-mCherry-IRES-Cre	Stanford Viral Vector Core	RRID: GVVC-AAV-165
AAV8-Ef1 α-DIO-RVG-WPRE-hGH-pA	BrainVTA	BHV12400145
AAV8-Ef1 α-DIO-H2B-EGFP-T2A-TVA-WPRE-hGH-pA	BrainVTA	PT-0021 r
RV-ENVA-ΔG-dsRed	BrainVTA	R01002

REAGENT or RESOURCE	SOURCE	IDENTIFIER
AAV5-hSyn-DIO-mCherry	Gift from Bryan Roth	RRID:Addgene_50459
Chemicals, peptides, and recombinant proteins		
Clozapine	Sigma-Aldrich	Cat #5786-21-0
CP154,526	Sigma-Aldrich	Cat #257639-98-8
Critical commercial assays		
Corticosterone ELISA Kit	Enzo	Cat #ADI-900-097
RNAscope Multiplex Fluorescent Reagent Kit v2	Advanced Cell Diagnostics	Cat #323100
Experimental models: Organisms/strains		
C57BL/6J	The Jackson Laboratory	JAX:000664
Grp ^{Cre}	Yu et al. (2017)	N/A
Grpr ^{iCre}	Munanairi et al. (2018)	N/A
Ai32	Madisen et al. (2012)	N/A
Ai9	Madisen et al. (2012)	N/A
Opn4 KO	Lucas et al. (2003)	N/A
Opn4 ^{Cre}	MMRRC	MMRRC_036544-UCD
Tra2β CKO	Diao et al. (2018)	N/A
Adcyap1 $^{f/f}$	Ross et al. (2018)	N/A
Adcyap1 ^{Cre}	Tan etal. (2016)	N/A
Oligonucleotides		
RNAscope® Probe- Mm-Grpr-C2	Advanced Cell Diagnostics	Cat #317871-C2
RNAscope® Probe- iCre-C3	Advanced Cell Diagnostics	Cat #423321-C3
RNAscope® Probe- Mm-Adcyap1r1	Advanced Cell Diagnostics	Cat #409561
RNAscope® Probe- Mm-Grp-C2	Advanced Cell Diagnostics	Cat #317861-C2
Adcyap1r1 siRNA	Sigma-sial	NM_001025372
Software and algorithms		
ImageJ	(Schindelin et al., 2012)	https://imagej.nih.gov/ij/
nVista Acquisition Software	Inscopix	https://support.inscopix.com/support/products/nvista

REAGENT or RESOURCE	SOURCE	IDENTIFIER
Inscopix Data Processing Software	Inscopix	https://support.inscopix.com/support/products/data-processing-software/inscopix-data-processing-software-introduction
MATLAB R2019a	MathWorks	https://www.mathworks.com/products/matlab.html
GraphPad Prism 9	GraphPad Software	https://www.graphpad.com/scientific-software/prism/
Origin 2015 software	OriginLab	https://www.any-maze.com/
ANY-maze	Stoelting	https://www.any-maze.com/
KlustaKwik	Kadir et al. (2014)	http://klustakwik.sourceforge.net/
NeuroScope	Hazan et al. (2006)	http://neurosuite.sourceforge.net/